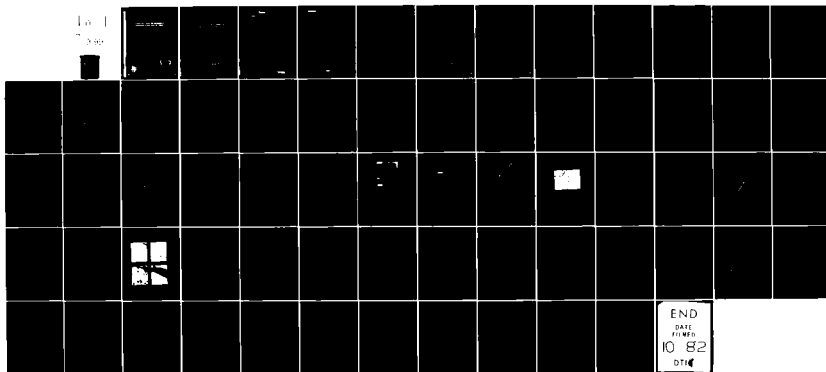


AD-A119 199 SOUTHWEST RESEARCH INST SAN ANTONIO TX F/G 20/11
STUDY OF FATIGUE MECHANISMS IN AEROSPACE STRUCTURAL MATERIALS. (U)
FEB 82 J LANKFORD, D L DAVIDSON, G R LEVERANT F49620-78-C-0022
AFOSR-TR-82-0699 NL

UNCLASSIFIED



END
DATE
FILED
10 82
DTIC

AD A119199

(1)

STUDY OF FATIGUE MECHANISMS IN AEROSPACE STRUCTURAL MATERIALS

by

James Lankford
David L. Davidson
Gerald R. Leverant
John E. Hack
Roy M. Arrowood

AFOSR ANNUAL REPORT

This research was sponsored by the Air Force Office of Scientific Research,
Directorate of Electronics and Solid State Sciences,
Under Contract F49620-78-C-0022

^{public}
Approved for release; distribution unlimited.

February 1982

DTIC
ELECTED
SEP 14 1982
S D
B

DTIC FILE COPY



**SOUTHWEST RESEARCH INSTITUTE
SAN ANTONIO**

HOUSTON

82 09 13 145

AFOSR-TR- 82-0699

STUDY OF FATIGUE MECHANISMS IN AEROSPACE STRUCTURAL MATERIALS

by

James Lankford
David L. Davidson
Gerald R. Leverant
John E. Hack
Roy M. Arrowood

AFOSR ANNUAL REPORT

This research was sponsored by the Air Force Office of Scientific Research,
Directorate of Electronics and Solid State Sciences,
Under Contract F49620-78-C-0022

public

Approved for release; distribution unlimited.

February 1982

Approved:



**U. S. Lindholm, Director
Department of Materials Sciences**

AIR FORCE OFFICE OF SCIENTIFIC RESEARCH (AFSC)
NOTICE OF TRANSMITTAL TO DTIC

This technical report has been reviewed and is
approved for public release IAW AFPL 193-12.
Distribution is unlimited.

MATTHEW J. KERPER
Chief, Technical Information Division

UNCLASSIFIED

SECURITY CLASSIFICATION OF THIS PAGE (When Data Entered)

REPORT DOCUMENTATION PAGE		READ INSTRUCTIONS BEFORE COMPLETING FORM
1. REPORT NUMBER AFOSR-TR- 82-0699	2. GOVT ACCESSION NO. AD-A119 199	3. RECIPIENT'S CATALOG NUMBER
4. TITLE (and Subtitle) Study of Fatigue Mechanisms in Aerospace Structural Materials	5. TYPE OF REPORT & PERIOD COVERED Annual Scientific Report 1 Jan 1981 - 31 Dec 1981	
7. AUTHOR(s) James Lankford David L. Davidson Gerald R. Leverant	6. PERFORMING ORG. REPORT NUMBER F49620-78-C-0022	
9. PERFORMING ORGANIZATION NAME AND ADDRESS Southwest Research Institute 6220 Culebra Road (P.O. Drawer 28510) San Antonio, TX 78284	10. PROGRAM ELEMENT, PROJECT, TASK AREA & WORK UNIT NUMBERS 61102F 2306/A1	
11. CONTROLLING OFFICE NAME AND ADDRESS AF Office of Scientific Research Bolling AFB, Building 410 Washington, DC 20332	12. REPORT DATE February 1982	
14. MONITORING AGENCY NAME & ADDRESS (if different from Controlling Office)	13. NUMBER OF PAGES 64	
	15. SECURITY CLASS. (of this report) UNCLASSIFIED	
	16. DECLASSIFICATION/DOWNGRADING SCHEDULE	
16. DISTRIBUTION STATEMENT (of this Report) Approved for public release; distribution unlimited		
17. DISTRIBUTION ST. (if different from abstract entered in Block 20, if different from Report)		
18. SUPPLEMENTARY		
19. KEY WORDS (Continue on reverse side if necessary and identify by block number) Fatigue Crack Initiation Crack Growth Aluminum Titanium Titanium Matrix Composites Hydrogen Embrittlement Crack Tip Plasticity Overloads Dwell Debit		
20. ABSTRACT (Continue on reverse side if necessary and identify by block number) This report summarizes the results of a three-phase study of (1) fatigue crack growth and load interaction modeling in aluminum alloys, (2) the effect of microstructure on susceptibility to hydrogen embrittlement in titanium alloys, and (3) micromechanisms of fatigue crack growth in titanium matrix composites. In the aluminum alloy phase of the work, crack tip strains and micromechanics have been determined using a new high resolution technique. These strains were used to evaluate which of several possible failure criteria (strain range, stress		

Continues

range, critical strain to fracture, cumulative damage, and critical work to failure) should be incorporated into a crack growth model. It was found that only the critical strain to fracture model was compatible with all of the observed crack tip parameters. In addition, progress was made in developing computational codes for transforming crack tip strains into the corresponding local stress fields; these results can be used in determining the residual stress fields caused by overloads.

In the titanium alloy phase, previous results had shown that the dwell-debit associated with beta heat-treated IMI-685 tested at room temperature was due to a hydrogen embrittlement phenomenon rather than a creep-fatigue interaction. Hydrogen enrichment due to diffusion to the hydrostatic stress field generated at the tip of a long, blocked shear band was found to be responsible for the embrittlement. The influence of microstructure has now been determined by conducting tests on three near-alpha alloys (IMI-685, IMI-829 and Ti-5Al-2.5Sn) and two alpha-beta alloys (Ti-6Al-4V and Ti-6Al-2Sn-4Zr-2Mo-0.1Si). It has been found that all of the near-alpha alloys are susceptible to hydrogen embrittlement during dwell fatigue while the alpha-beta alloys were immune when all five alloys were beta heat treated to the large colony microstructure. This behavior is associated with the fine, discontinuous nature of the beta plates in the near-alpha alloys as opposed to the thick continuous beta plates found in the alpha-beta alloys. Thick continuous beta plates serve to blunt any crystallographic microcracks which form in the alpha platelets because of the higher tolerance for hydrogen in the beta phase. In addition, results of interrupted sustained-load tests have shown the need for the attainment of a critical level of strain for embrittlement to occur and have confirmed that the intersection of slip bands and colony boundaries are the location of crack nucleation sites.

In the titanium matrix composite phase, the effect of heating the as-received B₄C coated boron fiber, Ti-6Al-4V matrix composite was to weaken the interface between matrix and fiber. In the heated material, there is a strong tendency for fatigue cracks to be deflected by this decohesion of the interface, so that the crack grows down this interface as opposed to across the fibers. Scanning Auger microscopy has revealed calcium segregation at the interface between B₄C and reaction zone, and atomic absorption analysis of the coated fibers has indicated that they may be the source of the calcium. Heat treatment weakens the fiber/matrix interface, evidently by calcium segregation, and thus promotes debonding of the fiber from the matrix. Crack tip strain analyses for matrix material at different cyclic stress intensity factors (ΔK) and for crack tip opening values of the same magnitude as previously measured in the as-received composite have been completed. Crack tip strains for the matrix material were then used to derive effective cyclic stress intensity factors (ΔK_{eff}) for fatigue cracks grown in the composite. These values were used to estimate crack growth rates, which agreed well with those actually measured.

TABLE OF CONTENTS

	<u>Page</u>
LIST OF ILLUSTRATIONS	v
LIST OF TABLES	vii
I. RESEARCH OBJECTIVES	1
A. Aluminum Alloy Phase	1
B. Titanium Alloy Phase	1
C. Titanium Matrix Composite Phase	1
II. STATUS OF THE RESEARCH EFFORT	2
A. Aluminum Alloy Task	2
1. Scope	2
2. Fatigue Crack Tip Strains in 7075-T6 by Stereoimaging and Their Use in Crack Growth Models	2
a. Introduction	2
b. Experimental Technique	2
c. Experimental Results	3
d. Crack Growth Models	9
(1) Critical Strain to Fracture Model	9
(2) Cumulative Damage Model	11
(3) Critical Work to Failure Model	13
e. Discussion	15
(1) Experimental Results	15
(2) Crack Growth Models	16
3. Calculation of Stresses from Strains Derived by Stereoimaging	18
4. References	18
B. Titanium Alloy Task	21
1. Introduction	21
2. Progress During Current Year	21
3. References	28
C. Titanium Matrix Composite Task	31
1. Introduction	31
2. Materials and Heat Treatments	31
3. Characterization of Interface	33
4. Fatigue Crack Propagation Resistance	36
5. References	50

TABLE OF CONTENTS (CONTINUED)

	<u>Page</u>
III. PUBLICATIONS (AFOSR SPONSORSHIP)	51
IV. PROGRAM PERSONNEL	54
V. INTERACTIONS (1981)	55

Accession For	
NTIS GRA&I	<input checked="" type="checkbox"/>
DTIC TAB	<input type="checkbox"/>
Unannounced	<input type="checkbox"/>
Justification	
By _____	
Distribution/	
Availability Codes	
Dist	Avail and/or Special
A	



LIST OF ILLUSTRATIONS

<u>Figure</u>		<u>Page</u>
1	Distribution of Maximum Shear Strain at $\Delta K = 6.2 \text{ MN/m}^{3/2}$	5
2	Crack Tip Plastic Strain Range Vs ΔK ; The Line Shown is Consistent with the Critical Strain Model	6
3	Crack Opening Displacement as a Function of Distance Behind the Crack Tip	7
4	Crack Tip Plastic Strain Range Vs Crack Tip Opening Displacement	8
5	Schematic of the Energy Change with ΔK Showing the Effect of Change in Crack Tip Deformation Mode	17
6	Distribution of Maximum Principal Stress Range, 7075-T6, $\Delta K = 8 \text{ MN/m}^{3/2}$; x and y in Micrometers	19
7	Distribution of the Maximum Stress in the Loading Direction (x) on the Next Loading Cycle After a 100% Single Overload	20
8	Comparison of TEM Micrographs of Beta-Phase Distribution in Three of the Alloys Studied	24
9	Hydrogen Assisted Crack Behavior in Large Colony Material .	26
10	SEM Fractograph of a Macroscopic Facet on the Static Load Specimen of Ti-6Al-2Mo-4Zr-2Sn-0.1Si Showing Ductile Tearing of the Beta Phase	27
11	Cracking in 400-Minute Specimen Showing Initiation of Cracking at Slip Band - Colony Boundary Intersections .	30
12	SEM Micrograph and Auger Elemental Maps of As-Received Amercom Composite, Fractured in the High Vacuum of the Microscope	34
13	Fatigue Specimen	37
14	Comparison of Fatigue Crack Paths in As-Received and Heat-Treated Composite Specimens	38
15	Variation of Crack Opening Displacement with Distance Behind the Crack Tip	39
16	Schematic of Crack Growth Through the Composite, Showing Measured Crack Growth Rates in the Lower Portion and the Location of Some of the Following Figures in the Upper Portion	40

LIST OF ILLUSTRATIONS (CONTINUED)

<u>Figure</u>		<u>Page</u>
17	Cyclic Range of Effective Strain at the Tip of a Fatigue Crack in Unreinforced Ti-6Al-4V, as a Function of the Applied Stress Intensity Factor Range	42
18	Maximum Shear Strain Range Distribution for a Fatigue Crack Grown at $\Delta K = 8 \text{ MN/m}^{3/2}$, Dry Environment, in Matrix Material; x and y in Micrometers	44
19	Maximum Shear Strain Range Distribution for a Fatigue Crack Grown in the Composite; Crack is Approximately 170 μm from Fiber	45
20	Maximum Shear Strain Range Distribution; Fatigue Crack Approximately 60 μm from Debonded (Cracked) Interface, Which is Shown by the Lines at About $y = 60 \mu\text{m}$	46
21	Maximum Shear Strain Range Distribution; Crack Tip Approximately 20 μm from an Uncracked Fiber/Matrix Interface, Shown as the Heavy Line at $y = 20 \mu\text{m}$	47
22	Maximum Shear Strain Which has Accumulated Near the Interface Region, Which is Approximately 20 μm Ahead of the Crack Tip	48
23	Distribution of Cumulative Normal Strains in the Direction Perpendicular to the Interface (EYY)	49

LIST OF TABLES

<u>Table</u>		<u>Page</u>
I	Crack Opening, Crack Tip Strain and Strain Distribution Parameters	4
II	Evaluation of the Cumulative Damage Integral	12
III	Computation of the Total Work Expended Per Unit Crack Growth	14
IV	Summary of Results of Dwell and Sustained Load Tests on All Alloys Studied to Date	22
V	Results of Interrupted Sustained Load Tests	29
VI	Materials and Heat Treatments	32
VII	Auger Electron Spectroscopy Results	35
VIII	Effective ΔK Experienced by Cracks in Composite at Applied ΔK of 22 MPa \sqrt{m}	43

I. RESEARCH OBJECTIVES

A. Aluminum Alloy Phase

1. Determine the plastic strain distribution in the region very close to the fatigue crack tip.
2. Incorporate crack strain information into fatigue crack growth models.
3. Establish the physical basis (criteria) for crack advance.
4. Develop a method for computing crack tip stress distributions for use in modeling overload retardation.

B. Titanium Alloy Phase

1. Establish the role of microstructure in the hydrogen embrittlement phenomena associated with the dwell debit in near-alpha titanium alloys.
2. Define the processes occurring in the early stages of hydrogen embrittlement to test the predictions of the micromechanical model developed to explain the dwell debit.

C. Titanium Matrix Composite Phase

1. Measurement of local matrix strains adjacent to the interface at the critical point when the interface breaks.
2. Chemically analyze the interfaces in material exposed to various heat treatments.
3. Model the effects of thermal processing treatments on crack propagation resistance by relating the interface chemistry to the critical condition for decohesion.

II. STATUS OF THE RESEARCH EFFORT

A. Aluminum Alloy Task

1. Scope

Two main areas of work have been emphasized, (1) the generation and use of crack tip strain data as the basis for fatigue crack growth models, and (2) the development of computer capabilities for calculating fatigue crack tip residual stress fields caused by overloads.

2. Fatigue Crack Tip Strains in 7075-T6 by Stereoimaging and Their Use in Crack Growth Models

a. Introduction

The development of a quantitative model which will predict the rate of growth of a fatigue crack can be divided into two subtasks. The first is to establish a quantitative criterion (failure condition) according to which the crack extends; the second is to quantify the extent of incremental crack advance (the distance over which the failure condition has been exceeded).

The present paper reports the results of an effort to bypass the intrinsic difficulties in dealing with crack tip "damage" in a microstructural sense, and instead, to quantify directly the very local crack tip deformation field. This information has been incorporated into quantitative crack growth models, and various predictions based on the models are compared with direct, in-situ SEM observations of the physically measurable factors related to crack extension. A failure criterion and the extent of crack advance are both extracted.

b. Experimental Technique

Cracks were grown at $6 < \Delta K < 10 \text{ MN/m}^{3/2}$ in a very dry environment, following which the specimen was transferred to the SEM loading stage [1] for high resolution dynamic and static observation. Photographs taken in the SEM in the unloaded and loaded conditions were then analyzed by the stereoimaging technique [2] to determine the displacements resulting from this loading change. Strains were then computed from the measured displacement distributions by differentiating the displacement functions in mutually perpendicular directions, thereby allowing determination of both the normal strains ϵ_{xx} and ϵ_{yy} , and the shear strain γ_{xy} . Principal strains were computed from these normal strains.

c. Experimental Results

Strain range distribution has been examined using a combination of the principal strains, i.e., the effective total strain range, defined here as

$$\Delta\epsilon_t^{eff} = \frac{2}{\sqrt{3}} (\Delta\epsilon_1^2 + \Delta\epsilon_1\Delta\epsilon_2 + \Delta\epsilon_2^2)^{1/2} \quad (1)$$

The strain ahead of the crack tip has been found to fit the function

$$\Delta\epsilon_t^{eff} = \Delta\epsilon_0 - m \ln(r+A) \quad (2)$$

where r = distance ahead of the crack tip and $\Delta\epsilon_0$, m , and A are constants used to fit the equation to the data. Values of the parameters characterizing the measured crack tip strain range are listed in Table I.

An example of the measured distribution of maximum shear strain near the crack tip is shown in Figure 1. The correlation between crack tip strain range $\Delta\epsilon_p$ and ΔK is shown in Figure 2. Considerable scatter exists in the data; this scatter may be understood by considering the crack tip opening displacements corresponding to the measured crack tip strains.

Several measurements of crack opening magnitude at various distances behind the crack tip are shown in Figure 3. These data, in agreement with similar information for 304SS obtained to within 1 μm of the crack tip, indicate that the crack opening displacement (COD) is a power function of the distance behind the crack tip, $-y$, so that

$$COD = C_0 |-y|^p \quad (3)$$

Values of C_0 and p are listed in Table I. From the data available, no correlation exists between p and ΔK ; the mean value and standard deviation is $p = 0.6 \pm 0.16$. However, correlation of C_0 with ΔK gives

$$C_0 = C \Delta K^q \quad (4)$$

where $C = 8 \times 10^{-11} \text{ m}$ and $q = 4.0$. This is a very useful and interesting result, since C_0 basically represents the crack tip opening displacement (at $y = 1 \mu\text{m}$ behind the tip).

By comparing C_0 and the crack tip plastic strain range value $\Delta\epsilon_p$, it is clear that the two are correlated, as shown in Figure 4. The correlating equation is

TABLE I
CRACK OPENING, CRACK TIP STRAIN AND
STRAIN DISTRIBUTION PARAMETERS

$$COD = C_0 | -y |^p$$

$$\Delta \epsilon_t^{eff} = \Delta \epsilon_0 - m \ln(y+A) \text{ ahead of crack}$$

Data Set	ΔK $MN/m^{3/2}$	Crack Tip			Strain Distribution			
		C_0 μm	p	$\Delta \epsilon_t(0)$	m	$\Delta \epsilon_0$	A μm	r_p^+ μm
34	6*	.15	.67	.040	.0068	.0416	1.26	175
35	6	.18	.64	.054	.0113	.0606	1.8	119
36	6.2*	.11	.60	.048	.0075	.0463	.76	200
39	8	.097	.72	.040	.0052	.0306	.15	100
40	8	.07	.77	.049	.0082	.0446	.59	104
41	8*	.25	.81	.094	.0310	.1372	4.0	64
43	10*	1.59	.34	.295	.0738	.2802	.81	40
44	10	.52	.60	.163	.0342	.1444	.58	56

* "Best" data.

^t r_p = value of r when $\Delta \epsilon_t^{eff} = .0065$.

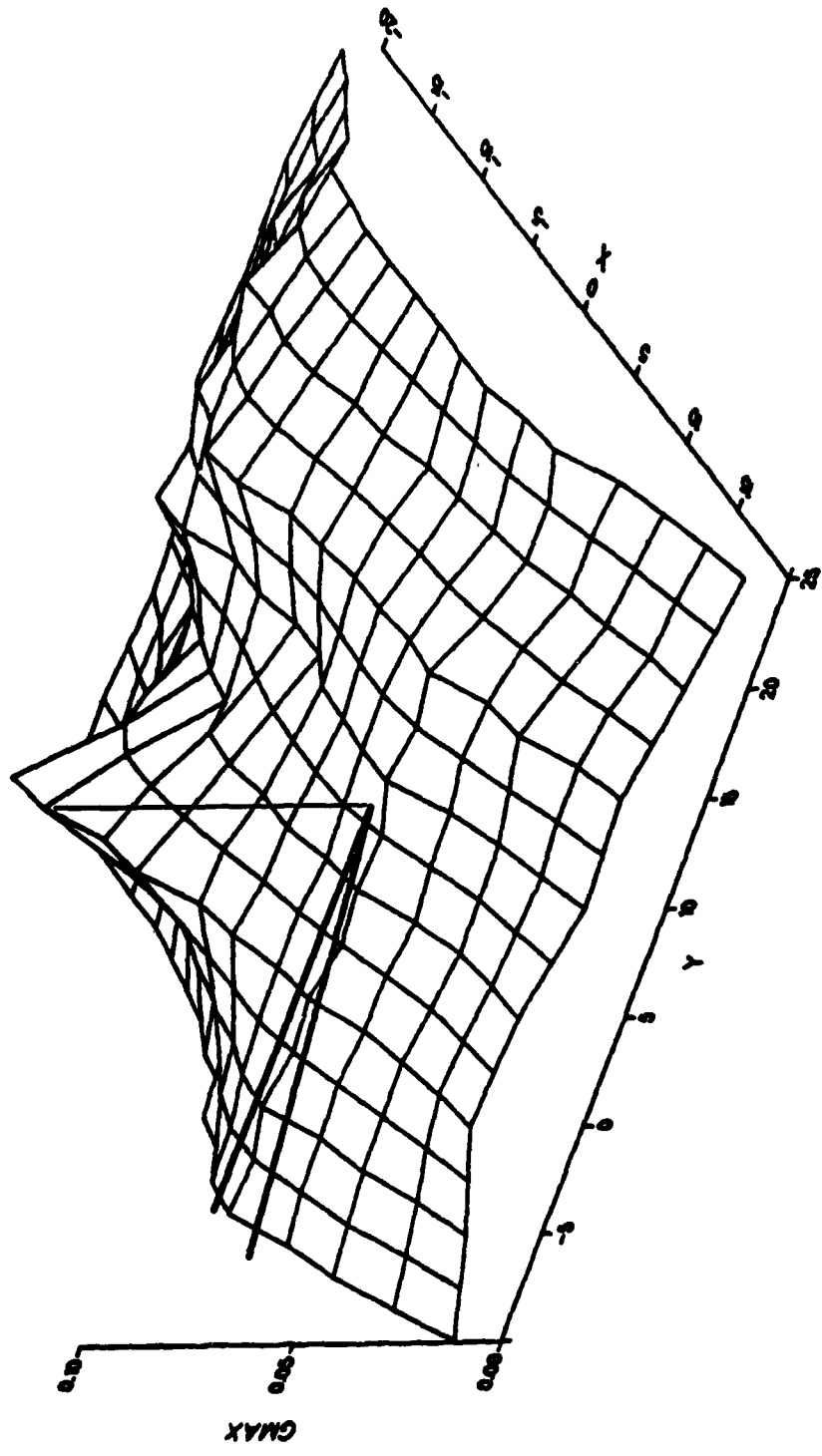


FIGURE 1. DISTRIBUTION OF MAXIMUM SHEAR STRAIN AT $\Delta K = 6.2 \text{ MN/m}^{3/2}$. Location of the crack is on the x-y plane. View is 35° around from the y-axis and 30° in elevation.

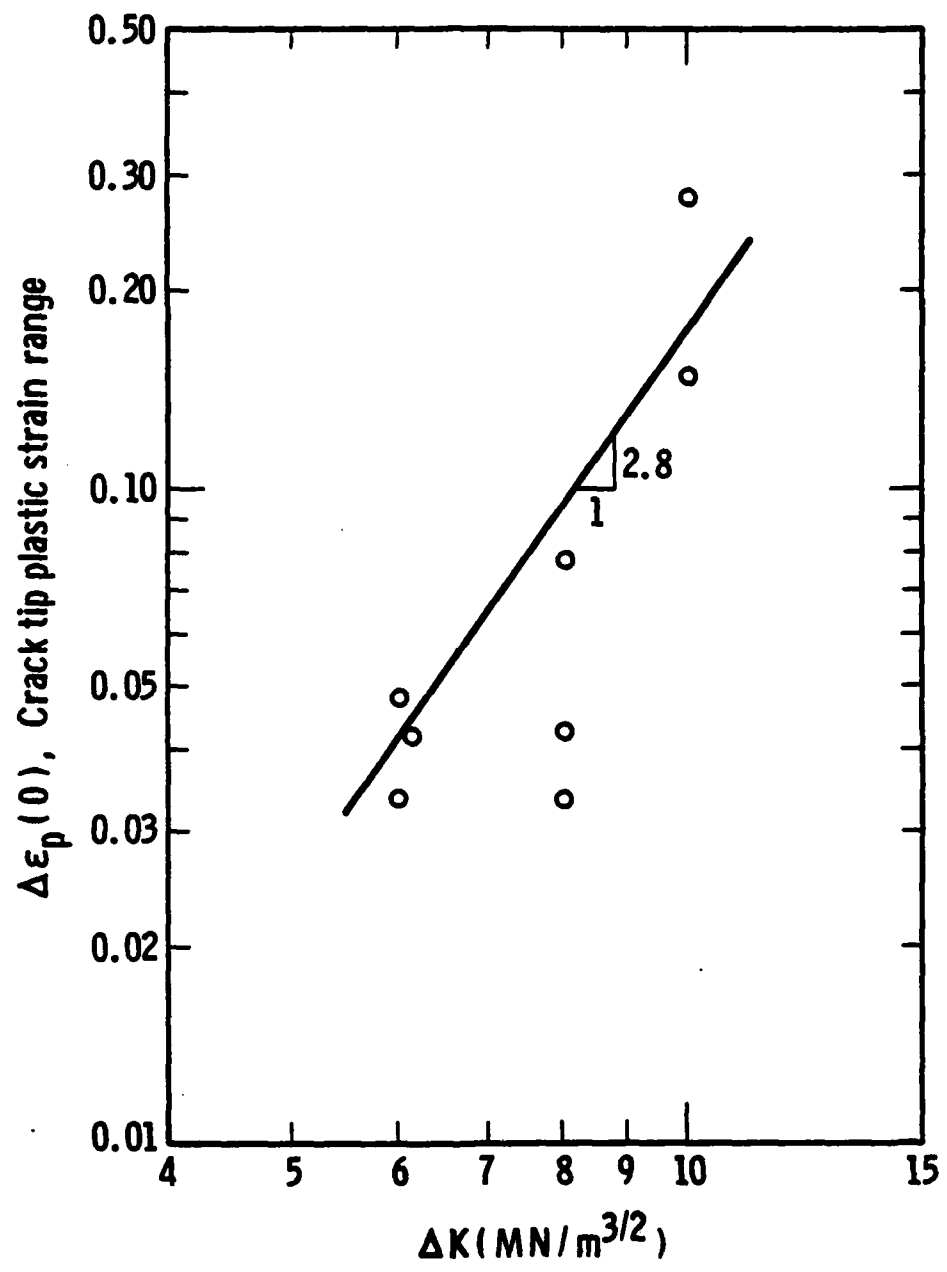


FIGURE 2. CRACK TIP PLASTIC STRAIN RANGE VS ΔK ; THE LINE SHOWN IS CONSISTENT WITH THE CRITICAL STRAIN MODEL.

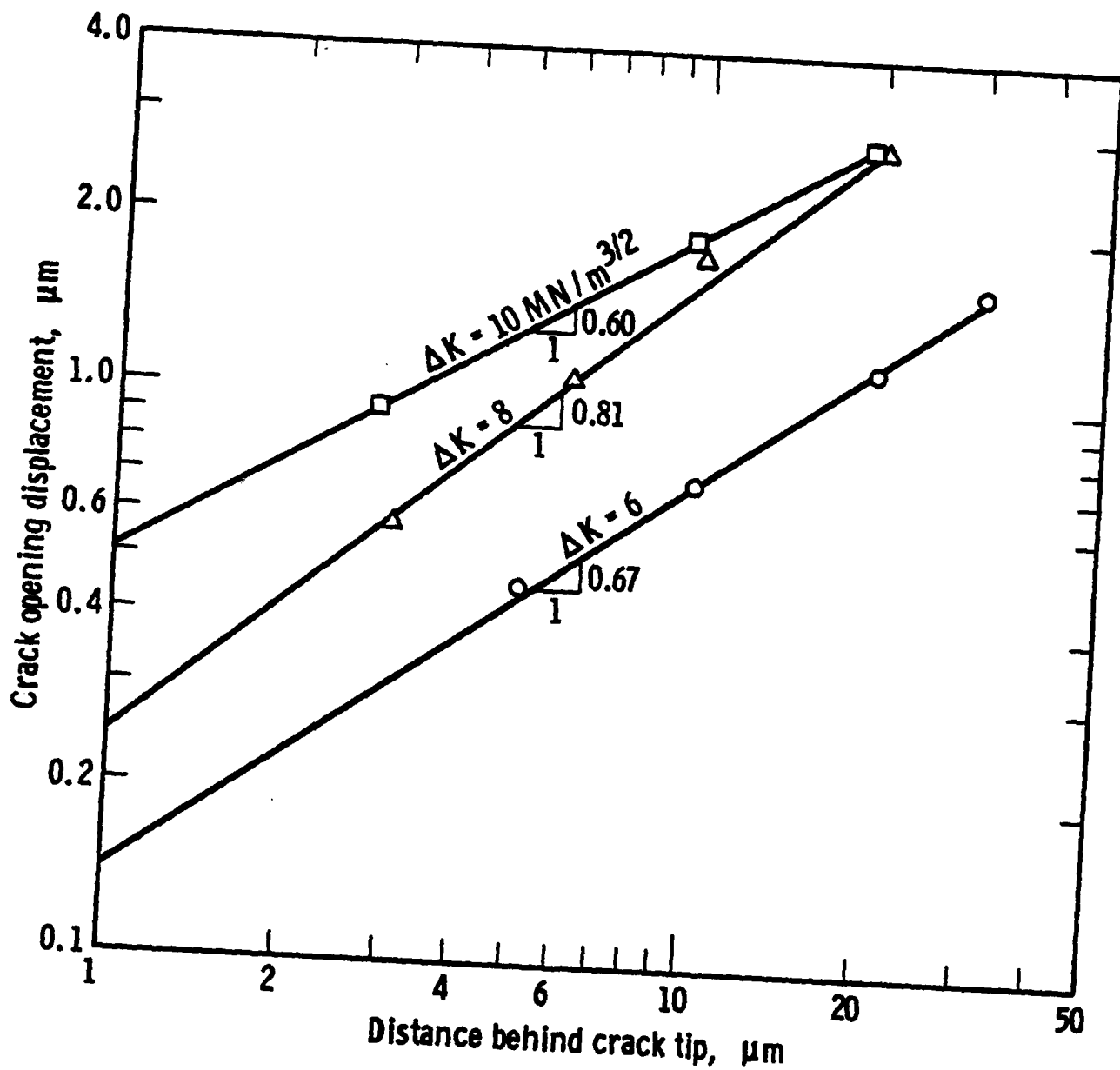


FIGURE 3. CRACK OPENING DISPLACEMENT AS A FUNCTION OF DISTANCE BEHIND THE CRACK TIP.

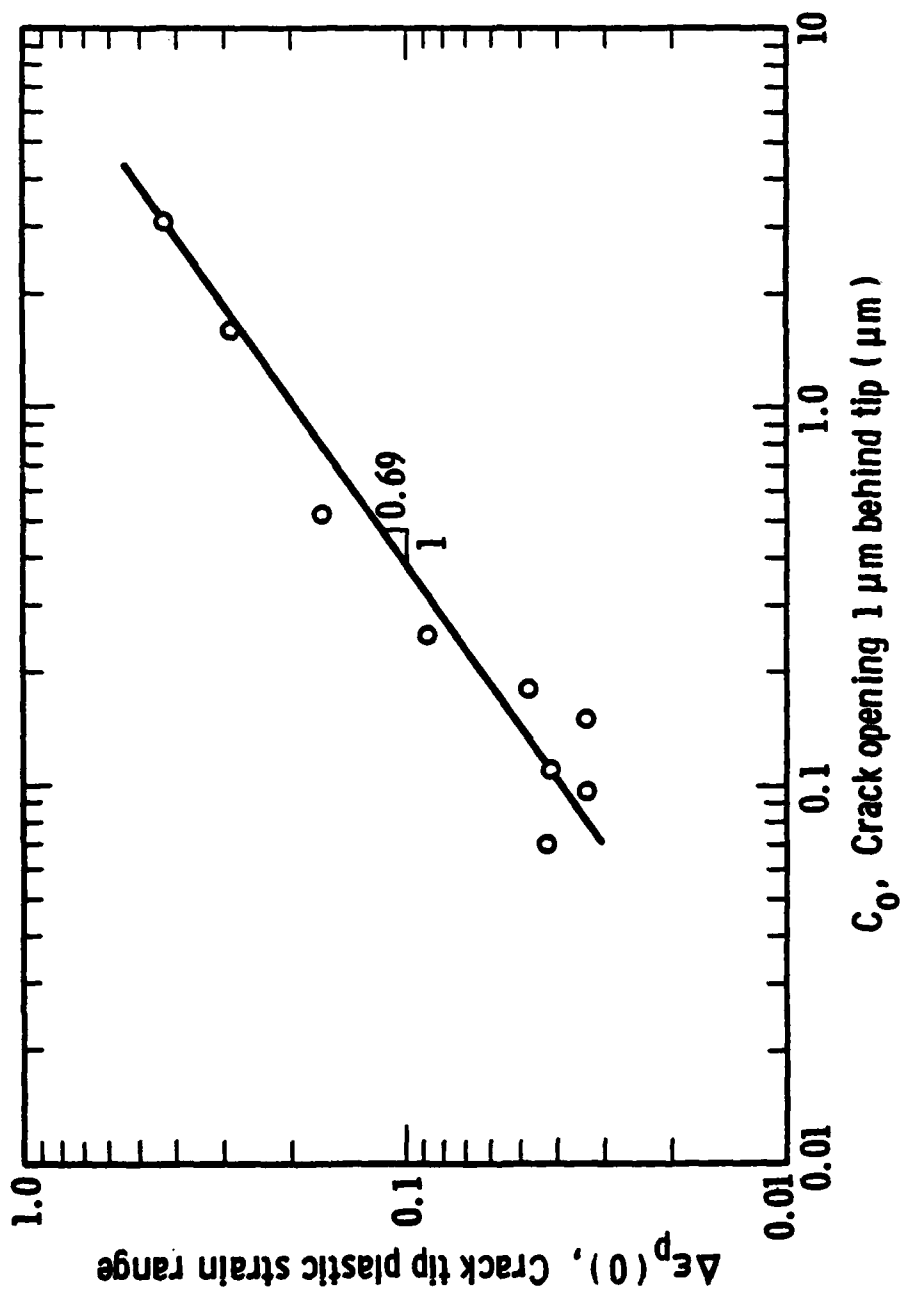


FIGURE 4. CRACK TIP PLASTIC STRAIN RANGE VS CRACK TIP OPENING DISPLACEMENT.

$$\Delta\epsilon_p = 2.8 \times 10^3 C_0^{0.69} \quad (5)$$

Combining Equations (4) and (5) gives

$$\Delta\epsilon_p = 2.8 \times 10^3 [C(\Delta K)^q]^{0.69} \quad (6)$$

From Figure 2,

$$\Delta\epsilon_p = K_0 (\Delta K)^r \quad (7)$$

For the above equations to be self consistent

$$K_0 = 2.8 \times 10^3 C^{0.69} \quad (8)$$

and

$$r = 0.69q \quad (9)$$

d. Crack Growth Models

The concept of a criterion for failure of an element at the crack tip has been postulated since the earliest studies of crack growth. Such failure criteria, for example, have considered incremental crack growth to occur upon the attainment of either a critical strain, a critical stress, or a critical energy, within a small region of material at the crack tip. The data presented in the figures and tables of this paper can be used to assess the relevance of these possible alternative failure criteria. Since crack tip strains are found to vary with ΔK , it follows that crack tip stresses are also ΔK dependent, hence neither is an adequate failure criterion.

The models developed here will examine both the attainment of a critical cumulative plastic strain at the crack tip as a criterion for crack advance, and also the concept of the necessity of expending a critical, cumulative amount of plastic work in order to extend the crack. A natural by-product of these calculations will be the predicted amount of incremental crack extension (directly related to crack growth da/dN) which occurs when the crack tip failure criteria are exceeded.

(1) Critical Strain to Fracture Model

Average crack growth per cycle da/dN (the usual macroscopically measurable parameter) is assumed to correspond to crack extension by an amount Δa after a critical number of cycles ΔN_c , so that

$$\frac{da}{dN} = \frac{\Delta a}{\Delta N_c} \quad (10)$$

The critical strain for fracture ϵ_c is reached when

$$\Delta N_c \Delta \epsilon_p = \epsilon_c \quad (11)$$

where $\Delta \epsilon_p$ = the plastic strain range experienced by the element Δa . Substituting, gives

$$\frac{da}{dN} = \frac{\Delta a \Delta \epsilon_p}{\epsilon_c} \quad (12)$$

If this relationship is valid, da/dN should vary with Δa and $\Delta \epsilon_p$, and these, like da/dN , must depend upon ΔK . In addition, the correlating term in the relationship, ϵ_c , must be independent of ΔK (constant). This requirement can be verified by solving Equation (12) for ϵ_c , substituting the appropriate ΔK -dependent relationships for Δa and $\Delta \epsilon_p$, and inserting for da/dN an empirical relationship in ΔK based on experiment. Determination of Δa requires the additional assumption that the incremental crack extension is proportional to the crack tip opening,

$$\Delta a = \alpha C_0 \quad (13)$$

Also,

$$\Delta a = \alpha C (\Delta K)^q \quad (14)$$

where $C = 7 \times 10^{-11}$ m and $q = 4.0$ (consistent with Equations (8) and (9) relating K_0 to C and r to q).

Macroscopic crack growth in the usual formalism is given by

$$\frac{da}{dN} = B(\Delta K)^s \quad (15)$$

where in the present case, $B = 1.3 \times 10^{-14}$ m/cy and $s = 6.8$. Also, in Equation (7) $K_0 = 2.8 \times 10^{-4}$ and $r = 2.7$. Solving Equation (12) for ϵ_c and inserting the functional relations for the other factors in the equation gives

$$\epsilon_c = \frac{\alpha C K_0}{B} \Delta K^{q+r-s} \quad (16)$$

Substituting the appropriate values for q , r , and s ,

$$\epsilon_c = \frac{\alpha C K_0}{B} \quad (17)$$

which is a constant, independent of ΔK . This result is encouraging evidence of the possible validity of critical cumulative strain as a criterion for crack growth. Substituting the values of C , K_0 and B given above into Equation (17), and assuming $\alpha = 0.5$ gives $\epsilon_c = 0.75$. This value is reasonable, considering the uncertainty in values of the constants. A similar evaluation of the Coffin-Manson related equation

$$\Delta\epsilon_p \Delta N_f^\beta = \epsilon_c \quad (18)$$

where $\beta = 0.5$, does not yield an ϵ_c independent of ΔK , and gives a numerical value of $\epsilon_c = 0.02$, much too low to be realistic.

(2) Cumulative Damage Model

This model presumes that a small element of material well ahead of the crack tip begins to accumulate damage as soon as plastic flow begins. The per-cycle strain range distribution ahead of the crack tip is $\Delta\epsilon(r)$; thus, the cumulative damage is represented by

$$\epsilon_{cd} = \frac{1}{da/dN} \int_0^{r_p} \Delta\epsilon(r) dr \quad (19)$$

where $\frac{dr}{da/dN}$ is the number of cycles experienced at the strain range during the period that the element is within the increment dr , and r_p is the plastic zone dimension. Substituting Equation (2) into (19) and integrating, gives

$$\epsilon_{cd}(da/dN) = r_p [\Delta\epsilon_0 + m(1 - \ln r_p)] \quad (20)$$

Numerical evaluation of the right side of this expression is given in Table II.

TABLE II
EVALUATION OF THE CUMULATIVE DAMAGE INTEGRAL

Data Set	$\Delta K^{3/2}$ MN/m	$\Delta \epsilon_0 r_p$ μm	$m(r_p+A) \ln(r_p+A)$ μm	mr_p μm	$\int \Delta \epsilon(r) dr$	$\frac{da}{dN}$ ($10^{-2} \mu\text{m/cy}$)
34	6	7.28	6.20	1.20	2.27	.15
35	6	7.21	6.54	1.34	2.02	.15
36	6.2	9.26	7.95	1.50	2.78	.2
39	8	3.06	2.40	0.52	1.18	1
40	8	4.64	3.96	0.85	1.50	1
41	8	8.78	8.89	1.96	2.05	1
43	10	11.2	11.1	2.96	2.97	5
44	10	8.10	7.80	1.90	<u>2.20</u>	5

Average = 2.12

Column 6 shows that the integral is nearly constant, so $\epsilon_{cd} \propto \frac{dN}{da}$ rather than being independent of ΔK . One is led to conclude from the numerical evaluation of this model that it does not yield reasonable results.

(3) Critical Work to Failure Model

This model provides a method for computing the work expended in growing the crack an incremental distance Δa , whereby the cracked area increases an amount Δa per unit depth into the material. By measuring, through stereoscopy, the cyclic strain at a point ahead of the crack tip, the corresponding energy dissipated in crack growth, W_c , can be calculated, based on push-pull tests of uncracked specimens cycled to saturation stress under strain-controlled conditions. Correlation of strain and work within the hysteresis loop for the smooth specimens gives

$$W_c = W_0 (\Delta \epsilon_p)^n \quad (21)$$

For 7075-T6, $W_0 = 1.3 \times 10^3 \text{ J/m}^3$ and $n = 1.06$.

The specific work, U , is the work expended per unit area of new crack, and is given by

$$U = \frac{W}{\Delta a} = \frac{W_0}{(\frac{da}{dN})} \sum_i (\Delta \epsilon_{p_i})^n d_i \quad (22)$$

Computational results for U are given in Table III using the cyclic strain data already presented.

Weertman [3] has shown theoretically that the relationship between crack growth rate, driving force (ΔK), material parameters, and U is

$$\frac{da}{dN} = A \frac{\Delta K^4}{\sigma_y^2 u U} \quad (23)$$

where u is the shear modulus, σ_y is the cyclic yield stress, and A is a constant. In this equation, it is assumed that U is a constant, and that da/dN is related to ΔK by a fourth power exponent, i.e., the crack is growing in the Paris regime. The data in Table III, however, show that in the present instance U is not independent of ΔK , suggesting that if an equation like (23) is to be used, a more general form should be employed

$$\frac{da}{dN} = A \frac{\Delta K^4}{\sigma_y^2 u U_0 (\Delta K)^m} = \frac{A (\Delta K)^{4-m}}{\sigma_y^2 u U_0} \quad (24)$$

where U_0 is an empirically determined constant.

TABLE III
COMPUTATION OF THE TOTAL WORK
EXPENDED PER UNIT CRACK GROWTH

<u>Set</u>	<u>ΔK (MN/m^{3/2})</u>	<u>$\frac{da}{dN}$ (10⁻⁸ m/cy)</u>	<u>$\sum (\Delta \epsilon_{p_i}^m) d_i$ (10⁻⁶ m)</u>	<u>W (10⁻³ J/m)</u>	<u>U (10⁵ J/m²)</u>
34	6	.15	1.19	1.6	10.6
35	6	.15	.71	.95	6.4
36	6.2	.2	1.3	1.75	8.7
39	8	1	.87	1.2	1.2
40	8	1	2.2	2.9	2.9
41	8	1	2.31	3.1	3.1
43	10	5	4.44	6	1.2
44	10	5	3.73	5	1.0

Note that in using this equation, the assumption is being made that the exponent on the driving force is equal to 4. Since da/dN is proportional to $(\Delta K)^{6.7}$, it is clear that $4-m = 6.8$, or $m = -2.8$. This means that

$$U = U_0 (\Delta K)^{-2.8} \quad (25)$$

Thus, the work expended per unit area of crack advance decreases with increasing ΔK .

Another equally valid way to consider this situation is to permit a variable driving force exponent. In this case, an even more general form of Equation (24) results,

$$\frac{da}{dN} = A \frac{\Delta K^n}{\sigma_y^m U_0 (\Delta K)^m} = A \frac{\Delta K^{n-m}}{\sigma_y^m U_0} \quad (26)$$

As noted before, da/dN is proportional to $\Delta K^{6.8}$. However, if the ΔK dependence of U is analyzed (Table III), it is found that a better representation than Equation (25) is

$$U = U_0 (\Delta K)^{-4.1}$$

Again, m is negative, but now the driving force exponent is only 2.7.

e. Discussion

(1) Experimental Results

The crack growth rate in the near-threshold region is less than would be implied by extrapolation of the Paris region, just as the CTOD is lower. This is a consequence of the changing mode of deformation from predominantly Mode I in the Paris region, to an increasingly Mode II-dominated mix, as ΔK is decreased toward threshold. This tendency suggests that much of the crack driving force is dissipated in shear strain, rather than in tensile (Mode I) opening of the crack; the amount of Mode I opening generally governs the amount of actual crack extension.

Some of the data presented in Table I is considered to be "best" for the purpose of characterizing the crack tip during crack extension. This judgement was based on the following: during the past four years, we have observed, at high resolution in the SEM, cracks growing in various aluminum alloys at relatively low stress intensities. It has become increasingly apparent that crack extension does not occur on

every cycle. Instead, as cycling progresses, the tip generally blunts to an ever increasing extent (but does not grow), while the crack tip opening likewise increases, until the crack extends upon reaching some critical state which our data suggest corresponds to a critical cumulative strain. This sharp-blunt sequence is then repeated. With this observation in mind, it is our opinion that the "best" strain and CTOD data are those which are the larger of the measured values for a given ΔK , since these values usually will be most characteristic of the critical condition just prior to crack extension.

(2) Crack Growth Models

The critical strain to fracture model and the cumulative damage models are very similar in concept. The cumulative damage model considers an element of material ahead of the crack tip to accumulate damage on each cycle as the crack tip moves toward the element. Conversely, the critical strain to failure model considers an element of material immediately ahead of the crack tip which is accumulating strain at approximately the cyclic strain range at the crack tip through sufficient cycles that the sum reaches a critical value, and the element breaks. Numerical evaluation of these two failure criteria indicates that the critical strain model, which gives a failure strain of about 75%, is more reasonable than the cumulative damage model, which yields a cumulative strain of >212%. The reason for this may be that the cumulative damage model assumes damage to occur equally at both low and high strains (when the product of strain range and number of cycles remains constant); evidently, this is a poor assumption. Examination of the strain distribution indicates that the strain is relatively low within the plastic zone, peaking strongly at the crack tip (Figure 1). This trend increases at higher ΔK . Thus, damage to the material is apparently likewise distributed. The size of the critical element in which strain is accumulating is given by Equation (13) as approximately half the crack tip opening displacement. This small element of material has been referred to as the "process zone" in other theoretical models.

An alternate way of utilizing strains at the crack tip is through the expression derived by Weertman [3], Equation (23), where stress and strain are combined into an energy term U. The seemingly curious observation, Table III, that U decreases with increasing ΔK has also been shown by Fine [4] for several aluminum alloys, and by Davidson [5] for low-carbon steel. The latter observation was explained in terms of the effects of crack opening mode on the mechanisms of energy dissipation, and the same general observations appear relevant to the aluminum alloys. The concepts are shown, schematically, in Figure 5. The range of the present measurements are in the near-threshold region A-B. The ΔK_{TH} is defined as the loading condition when U becomes extremely large, and, through Equation (23), da/dN becomes very small. The line ABC represents the decrease in U which would occur if the fatigue crack continued to keep the same mix of Mode I and Mode II as ΔK increased. But at some

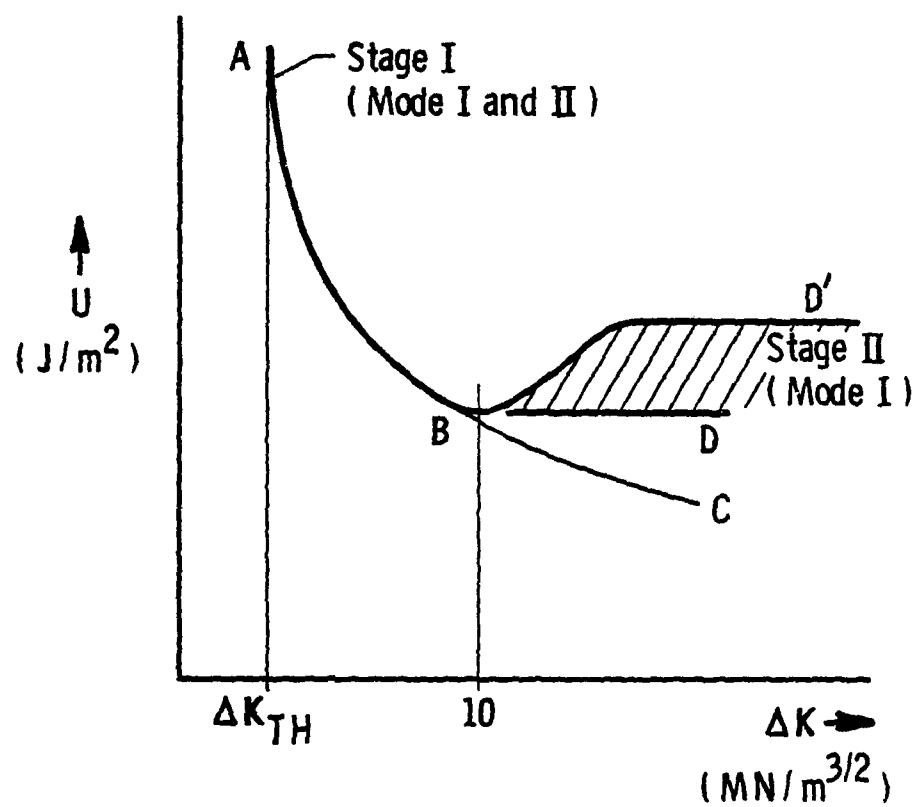


FIGURE 5. SCHEMATIC OF THE ENERGY CHANGE WITH ΔK SHOWING THE EFFECT OF CHANGE IN CRACK TIP DEFORMATION MODE.

point, B, the mode mix begins to change, with Mode I becoming much more dominant. At higher ΔK , the value of U may continue constant, as along line BD, or rise, as along line BD'. The latter change was observed in low-carbon steel; exactly what occurs for the aluminum alloys is not clear, but Fine's data [4] indicate some increase (as along BD') may also occur. The point of transition, B, is thought to be determined by the slip characteristics of the material, perhaps the stress state, and such metallurgical factors as grain size, shape, and texture. For 7075-T6 in the present study, $\Delta K = 10 \text{ MN/m}^3/2$ appears to be the beginning of the transition region, because the crack tip strain distribution (mode mix) is starting to change.

3. Calculation of Stresses from Strains Derived by Stereoimaging

The stereoimaging technique allows determination of three elements of the normal strain range tensor, and through the use of Mohr's circle, the principal strains and the maximum shear strain. By using the fact that the surface is in plane stress, it is also possible to compute the principal stresses and the maximum shear stress; the method is derived from that given by Lubahn and Felgar [6]. The only other information required is an equation relating stress to strain; these relations are often empirically derived for the appropriate situation (tension, compression, cyclic).

An example of the maximum principal stress field derived from 7075-T6, $\Delta K = 8 \text{ MN/m}^3/2$, is shown in Figure 6. Similar distributions for minimum principal stress, maximum shear stress, and mean stress are also available from the computations which produced this figure.

Residual stress developed by a single overload in 7075-T6 has also been computed. This has entailed computing the principal stresses on both the loading and unloading portion of the overload, resolving those stresses back into their normal stress components (x, y) and summing the resulting values. Although the results obtained to date are still being evaluated, the methodology and computational procedure have been developed. An example of the sum of the computed stresses on the next loading half-cycle following a 100% overload is given in Figure 7. This information has not yet been further interpreted.

4. References

- [1] Davidson, D. L. and Nagy, A., Journal of Physics E, V. 11, 1978, pp. 207-210.
- [2] Williams, D. R., Davidson, D. L., and Lankford, J., Experimental Mechanics, 20, 1980, pp. 134-139.
- [3] Weertman, J., Inter. J. Fracture, V. 9, 1973, pp. 125-131.
- [4] Liaw, P. K., Kwan, S. I., and Fine, M. E., Metallurgical Trans. A, V. 12A, 1981, pp. 49-55.

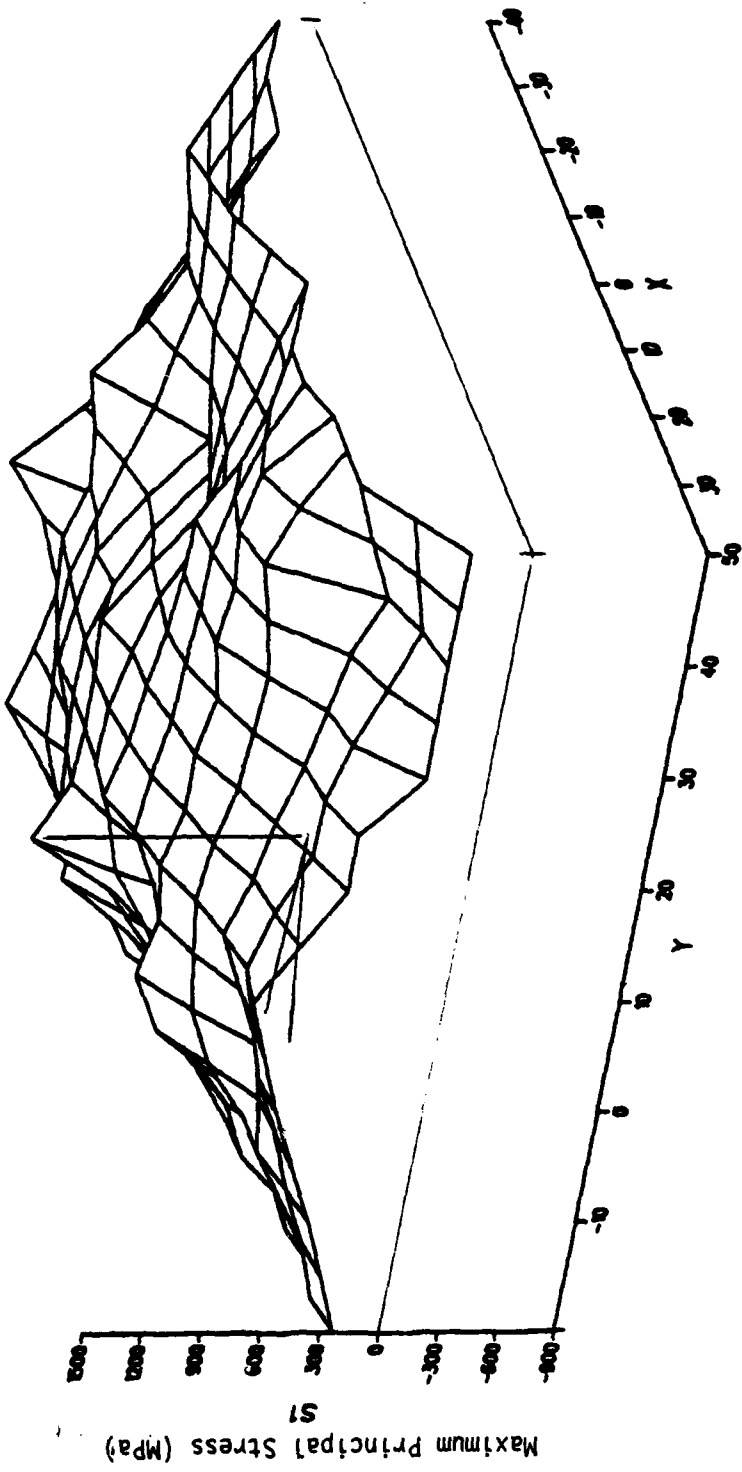


FIGURE 6. DISTRIBUTION OF MAXIMUM PRINCIPAL STRESS RANGE, 7075-T6, $\Delta K = 8 \text{ MN/m}^{3/2}$; X AND Y IN MICROMETERS. Crack is shown schematically on plane of zero stress. Load applied along x axis.

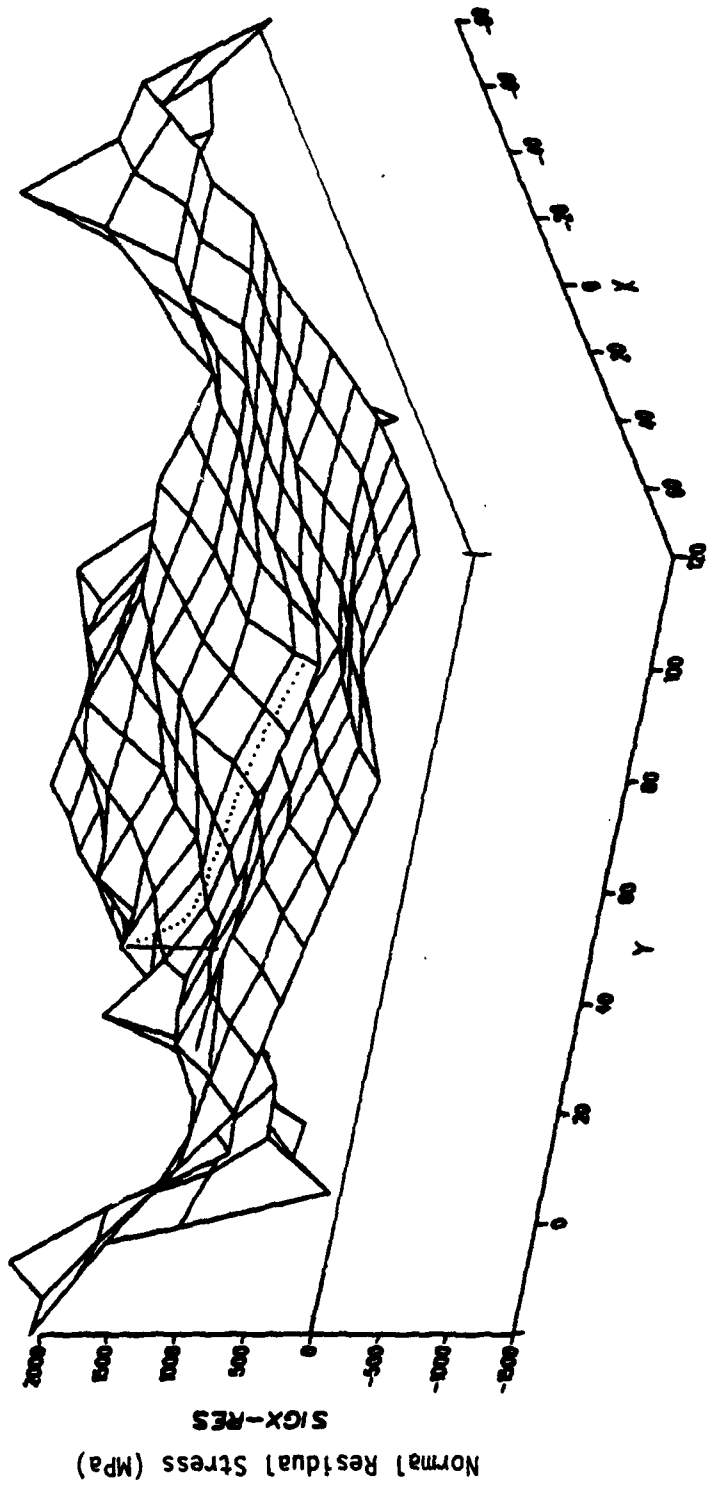


FIGURE 7. DISTRIBUTION OF THE MAXIMUM STRESS IN THE LOADING DIRECTION (x) ON THE NEXT LOADING CYCLE AFTER A 100% SINGLE OVERLOAD. This represents the sum of the stresses in the x -direction due to the overload cycle plus the stress due to the cycle after the overload. Comparing this to Figure 6 indicates a lack of stress peaking at and ahead of the crack tip. The dotted lines approximate the path of crack growth after the overload cycle.

- [5] Davidson, D. L., Fatigue of Engineering Materials and Structures, V. 3, 1981, pp. 229-236.
- [6] Lubahn, J. D. and Felgar, R. P., Plasticity and Creep of Metals, John Wiley, and Sons, Inc., New York, 1961, pp. 321-325.

B. Titanium Alloy Task

I. Introduction

Beta-processed near-alpha titanium alloys possess advantages both in reduced processing costs and crack propagation resistance. [1,2] However, the large grain size produced by beta-processing can lead to severe degradation of fatigue crack initiation resistance. [3] In addition, drastic reductions in low-cycle fatigue life and ductility have been observed in the near-alpha alloys IMI-685 (Ti-6Al-5Zr-0.5Mo-0.25Si) and 5-2.5 (Ti-5Al-2.5Sn) with the large colony microstructure when a five minute dwell period is introduced at peak stress. [4,5] The effects of a dwell period have been linked to the interaction of coarse, planar slip and internal hydrogen, even when the internal hydrogen levels are as low as 10 ppm. [6] The objective of this program is to define the microstructural features which control the crack initiation and embrittlement phenomena observed in these materials and use this information to develop processing techniques which allow the full exploitation of their potential advantages in cost, crack propagation resistance, and fracture toughness.

The approach to the problem includes dwell testing under load controlled conditions; measurement of the creep strains associated with dwell conditions; evaluation of the generic nature of the problem by testing several titanium alloys of similar microstructure; determination of the influence of hydrogen and beta phase distribution on the dwell effect; microchemical modeling of cleavage processes in titanium alloys; and exploratory process development aimed at simultaneously maximizing both fatigue crack initiation and propagation resistance.

2. Progress During Current Year

As reported at the end of the previous contract year, a model was developed to explain the interaction between creep deformation and internal hydrogen that appears to explain the formation of cleavage facets in IMI-685 under dwell and static load conditions. [7] The model ties these two factors together through the substantial hydrostatic stresses present near the tip of a stressed planar shear band.

Although the hydrostatic stresses are necessary for embrittlement, it was found that these stresses are not sufficient. This can be seen from the comparison in Table IV of results from tests on five alloys: IMI-685 (Ti-6Al-5Zr-0.5Mo-0.25Si); 5-2.5 (Ti-5Al-2.5Sn); IMI-829 (Ti-5.5Al-3.5Sn-3Zr-1Nb-0.25Mo-0.3Si); 6-4 (Ti-6Al-4V); and 6-2-4-2

TABLE IV
SUMMARY OF RESULTS OF DWELL AND SUSTAINED LOAD TESTS
ON ALL ALLOYS STUDIED TO DATE

<u>Alloy (Yield Strength, ksi (ppm H))</u>	<u>Type of Loading</u>	<u>Maximum Load (% Yield Strength)</u>	<u>Cycles to Failure</u>	<u>Plastic Strain to Failure (%)</u>
IMI-685 (127) (40)	Static Load	95	-	3.1
	5 Min. Dwell at Peak Load	95	173	3.0
	20 cpm	95	>30,000	-
	Tensile Test	-	-	6.9
5-2.5 (124) (90)	Static Load	95	-	3.7
	5 Min. Dwell at Peak Load	95	103	4.4
	20 cpm	95	12,303	-
	Tensile Test	-	-	8.5
IMI-829 (127) (32)	Static Load	95	-	2.1
	5 Min. Dwell at Peak Load	95	369	2.0
	Tensile Test	-	-	10.1
6-2-4-2 (125) (90)	Static Load	95	-	6.9
	5 Min. Dwell at Peak Load	100	178	6.4
	Tensile Test	-	-	5.5
6-4 (128) (60)	5 Min. Dwell at Peak Load	95	512	11.5
	Tensile Test	-	-	10.5

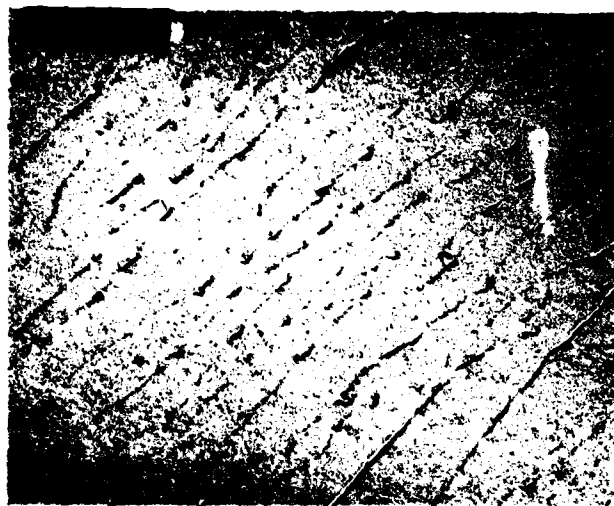
(Ti-6Al-2Sn-4Zr-2Mo-0.1Si). Of these alloys, the first three are considered near-alpha alloys while the latter two are alpha-beta alloys. The data shows that severe embrittlement is found in the near-alpha alloys under dwell or static load conditions, whereas the alpha-beta alloys are relatively immune.

This anomalous behavior can be explained by a closer examination of the microstructures of the alloys. A comparison of TEM replicas of three of the alloys is given in Figure 8. Although the general colony size is similar between the five alloys, it can be seen that there is a marked difference in beta distribution between the near-alpha and alpha-beta alloys. The lower percentage of beta phase in the near-alpha alloys is present in very fine, often discontinuous films along the alpha inter-lath boundaries. In the alpha-beta alloys, however, the beta is typically coarse and continuous.

It has long been recognized that the solubility of hydrogen in beta titanium is over an order of magnitude higher than that for the alpha phase. Also, the beta phase can apparently tolerate hydrogen levels close to its solubility limits without a significant loss of ductility or the onset of strain-induced hydride formation. [8,9] Thus, a thick, continuous layer of beta phase, which surrounds an alpha platelet, can act as a crack blunter if the alpha were to cleave. This is similar to the process described by Nelson [10] in his comparison of stress-corrosion cracking and hydrogen embrittlement in titanium alloys. The alpha platelet spacing is fine enough on an absolute scale that the stress intensity of one or even several small cleavage facets found near the tip of a blocked shear band would not be high enough to bring about ductile failure of the beta phase surrounding them. If the beta phase is very fine, or discontinuous, it will not present an effective barrier to alpha cleavage and, indeed, a crack may be able to follow a path that lies almost entirely in the embrittled alpha phase. A schematic drawing depicting this situation is shown in Figure 9. Examples of the beta phase acting as a ductile barrier to crack propagation were observed in macroscopically flat facets in specimens of the alpha-beta alloys (Figure 10).

The model predicts nucleation of hydrides and subsequent cracking at the intersection of planar shear bands and colony boundaries. Fractures of dwell specimens of IMI-685 and IMI-829 were sectioned perpendicular to the fracture surface and carefully polished to reveal the microstructure just under the initiation sites of cleavage facets. In both cases, colony boundaries were the only significant microstructural feature at the initiation site. Significantly, no defects were found at the initiation sites.

Three specimens of IMI-685 were held at 95% of yield stress for 200, 400 and 600 minutes, respectively. They were subsequently sectioned and polished to determine the occurrence and onset of cracking. This data was correlated with acoustic emission activity. The resonant-type transducer only allowed detection of high energy events without any form

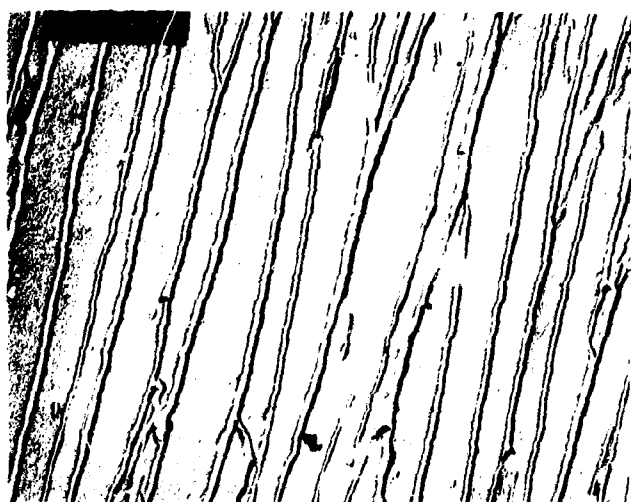


(a) IMI-685, 3600X.



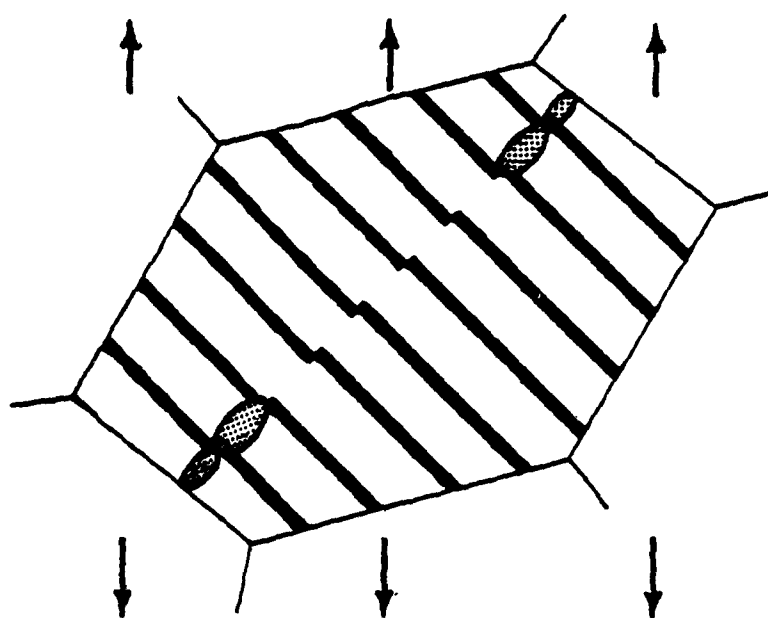
(b) IMI-829, 3600X.

FIGURE 8. COMPARISON OF TEM MICROGRAPHS OF BETA-PHASE DISTRIBUTION IN THREE OF THE ALLOYS STUDIED.

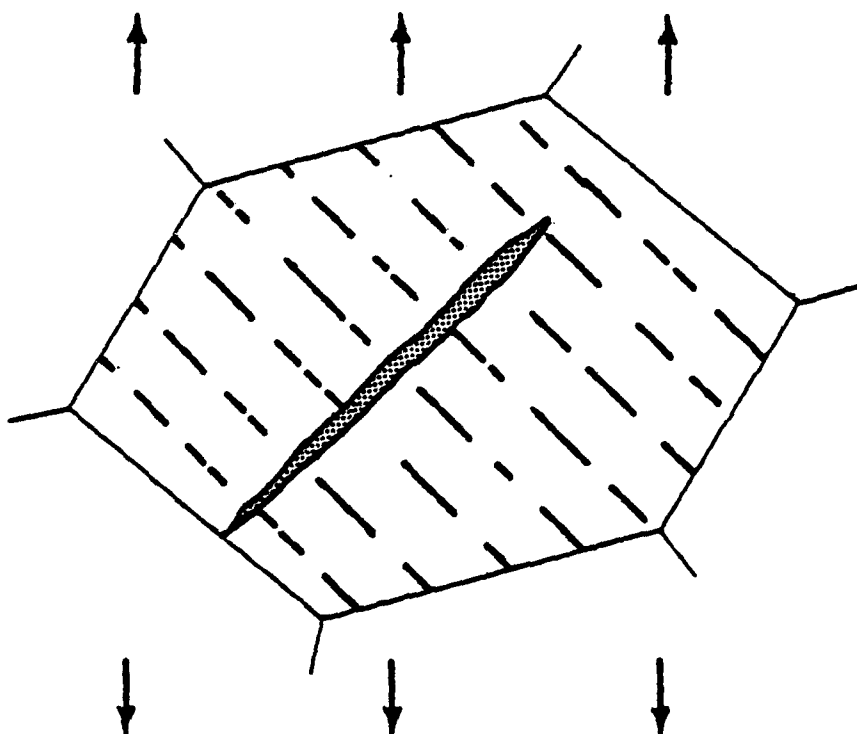


(c) 6-2-4-2, 3600X.

FIGURE 8 (CONTINUED). COMPARISON OF TEM MICROGRAPHS OF BETA-PHASE DISTRIBUTION IN THREE OF THE ALLOYS STUDIED.



(a) Crack Blunted by Thick Continuous Beta Phase.



(b) Crack Able to Propagate in Embrittled Alpha Phase.

FIGURE 9. HYDROGEN ASSISTED CRACK BEHAVIOR IN LARGE COLONY MATERIAL.

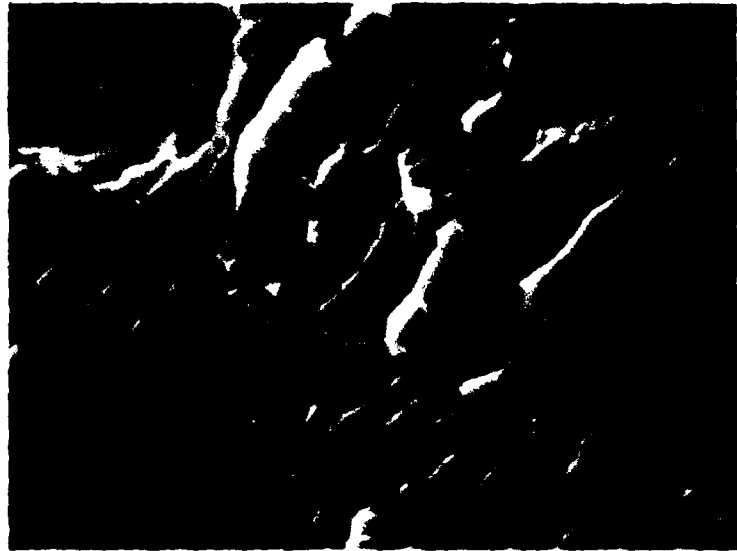


FIGURE 10. SEM FRACTOGRAPH OF A MACROSCOPIC FACET ON THE STATIC LOAD SPECIMEN OF Ti-6Al-2Mo-4Zr-2Sn-0.1Si SHOWING DUCTILE TEARING OF THE BETA PHASE.

of signature evaluation. As can be seen from the data in Table V, only the 400-minute specimen showed evidence of internal cracking. The three main areas of cracking found in the specimen correlate well with acoustic emission events detected at 0.8, 1.1 and 1.6% plastic strain. The fact that cracking only occurred in the specimen with over 1.0% plastic strain indicates that a critical strain, plus a critical hydrostatic stress, is required in addition to the time dependent diffusion of hydrogen.

Metallographic examination of one of the areas of internal cracking revealed that parallel cracks were emanating from a colony boundary (Figure 11). One of the cracks extended all the way across the colony while the other ended a short distance from the boundary. In both cases, as marked by arrows in Figure 11, planar slip bands extend across the colony and impinge on the boundary at precisely the point where the crack intersects the boundary. This is exactly what the model predicts.

3.0 References

- [1] Eylon, D., Pierce, C. M., and Hall, J. A., Metals Eng. Quant., Vol. 16, No. 1, 1976, p. 33.
- [2] Eylon, D., Hall, J. A., Pierce, C. M., and Ruckle, D. L., Met. Trans. A, Vol. 7A, 1976, p. 1817.
- [3] Lucas, J. J. and Konieczny, P. P., Met. Trans., Vol. 2, 1971, p. 911.
- [4] Eylon, D. and Hall, J. A., Met. Trans. A, Vol. 8A, 1977, p. 981.
- [5] Lankford, J., Davidson, D. L., and Leverant, G. R., Study of Fatigue Mechanisms in Aerospace Structural Materials, Annual Report on Contract F49620-78-C-0022, March 1979.
- [6] Evans, W. J. and Gostelow, C. R., Met. Trans. A, Vol. 10A, 1979, p. 1837.
- [7] Hack, J. E. and Leverant, G. R., Scripta Met., Vol. 14, 1980, p. 437.
- [8] Buck, O., Thompson, D. O., Paton, N. E., and Williams, J. C., Proceedings of 5th International Conference on Internal Friction and Ultrasonic Attenuation in Crystalline Solids, 1973, Aachen, Germany.
- [9] Williams, J. C. and Paton, N. E., unpublished research, Rockwell International, 1973.
- [10] Nelson, H. G., in Hydrogen in Metals, American Society for Metals, 1974, p. 445.

TABLE V
RESULTS OF INTERRUPTED SUSTAINED LOAD TESTS

<u>Minutes at Peak Load</u>	<u>Total Plastic Strain (%)</u>	<u>Number of Acoustic Emission Events Detected</u>	<u>Number of Areas of Cracking Found</u>
200	0.84	0	0
400	1.75	3	3
600	0.90	0	0

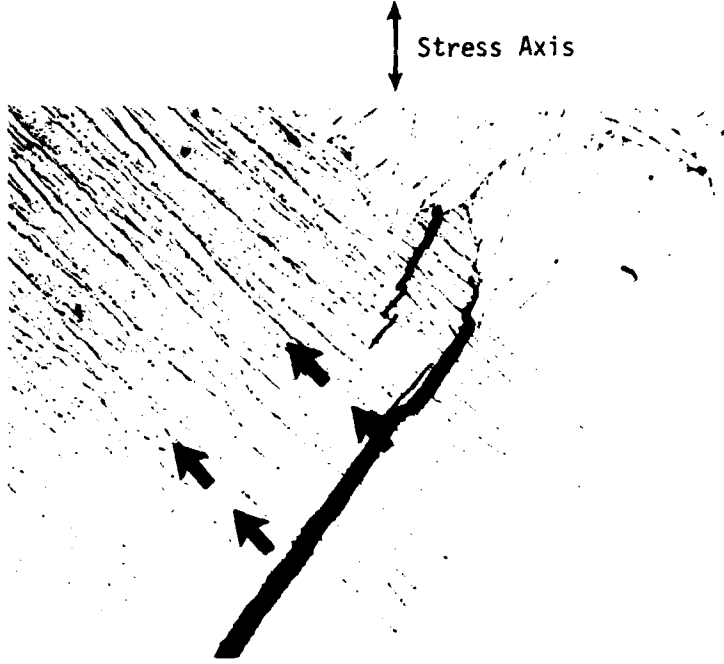


FIGURE 11. CRACKING IN 400-MINUTE SPECIMEN SHOWING INITIATION OF CRACKING AT SLIP BAND - COLONY BOUNDARY INTERSECTIONS. 500X.

C. Titanium Matrix Composite Task

1. Introduction

Fiber-reinforced metal matrix composites are promising materials for stiff, strong, and lightweight structures for aerospace applications. Excellent longitudinal strength and stiffness are readily obtained in these composites, provided that the bonding between strong, high-modulus fibers and ductile matrix is adequate. However, improved resistance to transverse fatigue crack propagation may require that the interface between fiber and matrix debond in the stress field of an approaching fatigue crack, thus deflecting the crack to a longitudinal direction so it will not break the reinforcing fibers. Successful applications of these materials may, consequently, hinge on the ability to optimize interface strength for controlled decohesion without degradation of transverse or longitudinal tensile strength. Careful control of thermal processing may be the most direct method of adjusting the interface strength.

The purpose of this task is to relate the strength of the fiber-matrix interface to the growth of a fatigue crack through the composite. Thermal processing is being used to degrade the interfacial strength. The effort to quantify the relationship between interfacial strength and crack growth utilizes two analytical techniques, both having high-spatial resolution: scanning Auger microprobe (SAM) of interfaces broken open in the high vacuum of that instrument for determination of the elements present in the interfacial region, and stereoimaging [1] of the crack tip regions for quantifying the local strains at which the interface breaks. Detailed observations of the crack-interface interaction are being made at high resolution using a fatigue stage which fits within the scanning electron microscope that was designed and constructed at SwRI. Use of these two techniques on material which has received various heat treatments is expected to clarify the effect of thermally induced changes in interfacial bonding and chemistry on fatigue crack growth.

2. Materials and Heat Treatments

Most of the effort has been on a panel of Ti-6Al-4V alloy reinforced with 5.6-mil fibers of B₄C-coated boron. This panel was fabricated by the standard diffusion bonding process at Amercom, Inc. The material has been tested in the as-received condition and after several different heat treatments, listed in Table VI. The heat treatment at 500°C (932°F) in vacuum was intended to produce an intermediate degradation of the interface adherence, in accordance with the experience of Mahulikar [2], who used this same heat treatment on another plate of identical material.

A limited amount of work has also been done on Ti-6Al-4V reinforced with B₄C/B fibers and on the same metal reinforced with SiC (SCS-6) fibers, both produced by Avco.

TABLE VI
MATERIALS AND HEAT TREATMENTS

<u>Fiber Material</u>	<u>Fiber Material</u>	<u>Manufacturer</u>	<u>Code</u>	<u>Heat Treatment Description</u>
B/B ₄ C	Ti-6Al-4V	Amercom	AR	As Received
B/B ₄ C	Ti-6Al-4V	Amercom	HT899	899°C (1650°F), vacuum (<10 ⁻⁶ torr), 4.5 h
B/B ₄ C	Ti-6Al-4V	Amercom	HT593	593°C (1100°F), air, 7 days
B/B ₄ C	Ti-6Al-4V	Amercom	HT500	500°C (932°F), vacuum, 7 days
B/B ₄ C	Ti-6Al-4V	AVCO	AR	As Received
SiC (SCS-6)	Ti-6Al-4V	AVCO	AR	As Received

3. Characterization of Interface

As described in the previous Annual Report, the reaction zone in the material used in this investigation has the typical structure [3-7] consisting of an inner sheath and radiating needles. Since fiber/matrix debonding occurs at the interface between the B₄C coating and the reaction zone, this program has concentrated on characterization of this interface. Surface chemical analysis of the interface was carried out on samples of Ti/B₄C/B composite as received and after each of the three heat treatments. The samples were fractured in the ultra-high vacuum (1.3×10^{-10} torr) of a Physical Electronics Model 595 high-resolution scanning Auger microscopy (SAM) system to expose the fiber/matrix interface for analysis. Maps and line scans were corrected for specimen topography. Published sensitivity factors [8] were used to convert Auger intensity ratios to quantitative area coverages. Further details of the Auger microscopy are given in reference [9].

Part of the fracture surface of the as-received Amercom composite is shown in Figure 12. The field of view includes the surface of a fiber and the trough where an adjacent fiber has pulled out of the matrix during fracture. A sliver has broken from the fiber, giving SAM access to the B₄C coating and B fiber interior as well as the surface. Figure 12 also contains SAM maps of the calcium, boron, and titanium concentrates of the same field of view.

The boron and titanium maps delineate the boron fiber and boron carbide coating and the metal matrix. The calcium map shows a significant concentration of calcium on the fiber and trough surfaces indicating segregation of this element at the fiber/matrix interface along which fracture occurred. Such calcium segregation also existed in the three heat-treated specimens. Table VII indicates the results of quantitative Auger analyses of points on the fiber surface and the trough in each of the four material conditions. The table also lists the sputter time for a reduction of the calcium concentration to a quarter of its surface value, and the corresponding approximate thickness of the Ca-enriched layer. The fiber-surface concentration of calcium is higher in the heat-treated materials than in the as-received sample. The trough-surface concentrations are less consistent, but for the 500°C and 593°C heat treatments there appears to have been an increase of interfacial segregation of calcium. The calcium segregation depth of 2.7 nm in the as-received material falls to a consistent 0.6-0.7 nm in all three heat treatments.

The source of the calcium is not yet certain, but a preliminary atomic absorption measurement revealed that the calcium content of the fibers prior to incorporation in the composite was about 270 ppm by weight. Further work on the origin of the calcium and its redistribution during heat treatment is planned.

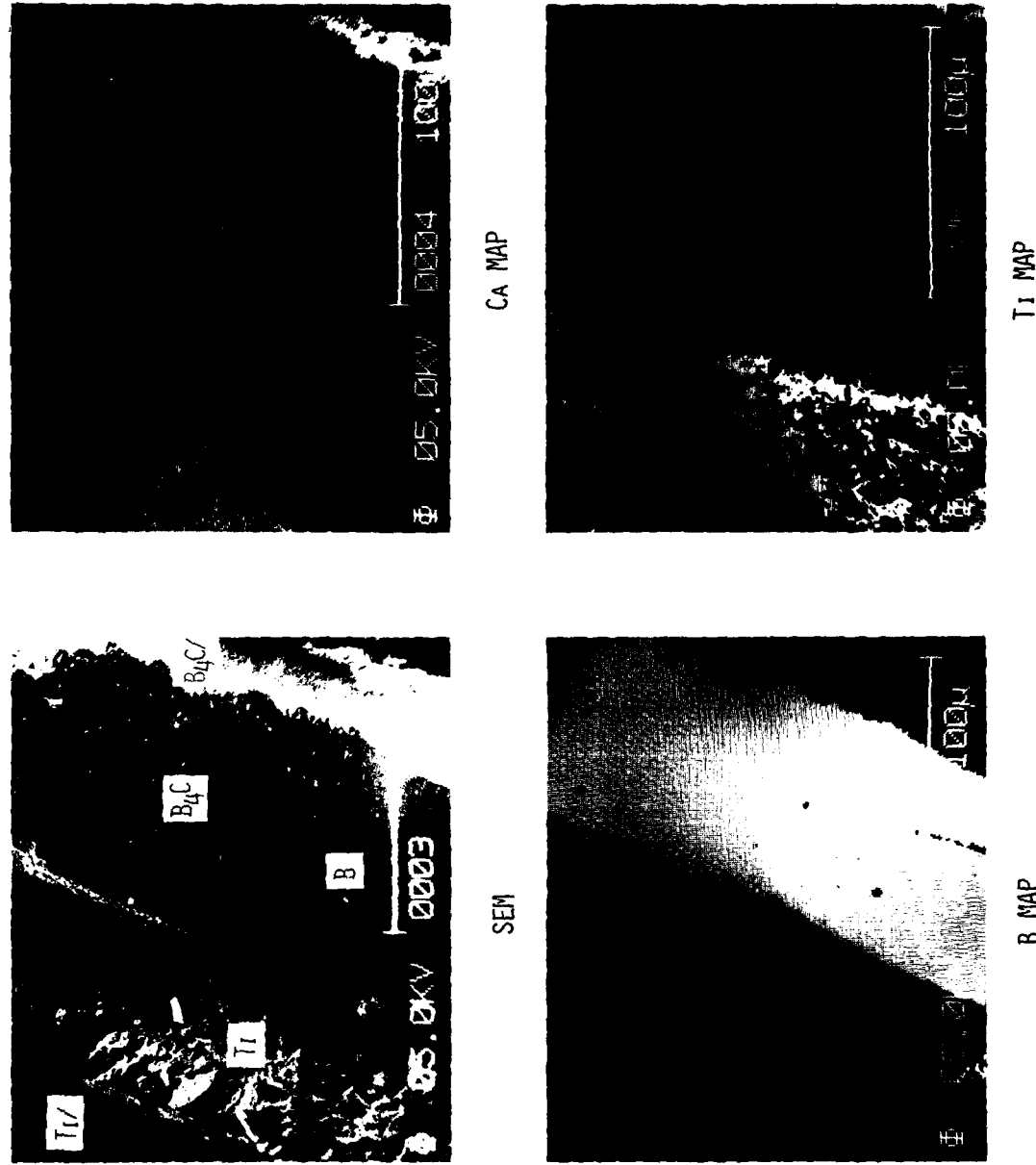


FIGURE 12. SEM MICROGRAPH AND AUGER ELEMENTAL MAPS OF AS-RECEIVED AMERCOM COMPOSITE, FRACTURED IN THE HIGH VACUUM OF THE MICROSCOPE. (Ti, titanium alloy matrix; B, boron fiber; B₄C, boron carbide coating; B₄C, fiber side of broken fiber/matrix interface; Ti/, matrix side of interface.)

TABLE VII
AUGER ELECTRON SPECTROSCOPY RESULTS

		<u>As-Fabricated</u>	<u>500°C</u>	<u>593°C</u>	<u>899°C</u>
Fiber Surface (Atomic %)	Ca	6.3	7.8	11.1	10.5
	B	65.5	59.1	59.7	58.2
	C	24.9	28.3	24.9	29.5
	Ti	1.7	1.2	1.1	0.8
	O	1.3	3.6	2.5	1.0
	V	0.3	< 0.1	0.7	< 0.1
Fiber Trough (Atomic %)	Ca	8.7	11.3	9.5	7.8
	B	40.1	36.3	29.4	50.6
	C	15.2	11.9	12.3	16.6
	Ti	29.3	35.3	33.6	23.5
	O	5.4	4.2	13.6	1.0
	V	1.3	1.1	1.6	0.5
Sputter Time for 75% Ca Reduction on Fiber (Min.)		5.4	1.1	1.3	1.3
Approx. Ca Segregation Depth (nm) on Fiber Surface		2.7	0.6	0.7	0.7

4. Fatigue Crack Propagation Resistance

In order to accomplish another objective of this task, measurement of critical local strains for decohesion, fatigue tests were run under close microscopic scrutiny. The specimens consisted of rectangular coupons with spark-cut edge notches (Figure 13). Careful hand polishing of the coupon surfaces revealed the reaction zones of the outermost layer of fibers, so that crack behavior could be related to position with respect to subsurface fibers. After cutting of the edge notch, titanium reinforcing tabs were spot welded to the grip regions. Fatigue loading was performed at 5-10 Hz with $R = 0.1$, and the load amplitude was adjusted periodically to keep ΔK constant as the crack grew.

Fatigue tests have revealed a distinct change in the crack propagation behavior in the three heat-treated materials as contrasted to the as-received composite. In the as-received composite, the crack propagated perpendicular to the fibers, with little deflection at fiber intersections. In the heat-treated samples, however, crack branching was typical of the interaction between the propagating crack and the interfaces (Figure 14). This deflection of the transverse crack by interface splitting resulted in reduced transverse crack propagation rates. Thus, in one test of HT899°C material, 1.8×10^6 cycles at a ΔK of 22 to 26 $\text{MPa}\sqrt{\text{m}}$ were necessary to propagate the crack across four successive fibers. In contrast, to propagate a crack through four fibers in the as-received material took only 66,000 cycles at 20 to 22 $\text{MPa}\sqrt{\text{m}}$. It is evident that fiber/matrix interface splitting was easier in the heat-treated materials, and that this had a profound effect on the crack path and the transverse crack propagation rate. The effect of all three heat treatments used so far is similar, and the effect is so strong that it poses problems for local strain measurements. The crack becomes so branched that it becomes impractical to monitor events at all the individual crack tips, and the stress intensity experienced by any one crack tip is no longer known.

It is instructive to compare the behavior of cracks in the composite to the behavior of cracked, unreinforced Ti-6Al-4V. Experimental data are now available on samples of this alloy which were produced by hot-pressing of foils to duplicate the processing history of the titanium matrix in the composites. Fatigue tests were run in the SEM fatigue stage at various ΔK values, and the crack opening displacements and crack-tip strains were measured by stereomicroscopy. Figure 15 shows the variation of crack opening displacement (COD) with distance from the crack tip. Included are data from the matrix material (i.e., Ti-6Al-4V with no reinforcing fibers) at three different ΔK levels and data from the as-received composite at 22 $\text{MPa}\sqrt{\text{m}}$. A sketch of the crack path (Figure 16) in the composite allowed correlation of the COD data sets with the position of the crack tip. The matrix material data fell on three straight, nearly parallel lines. The crack opening displacements of cracks in the composite, when the crack tips were not near a fiber, also fell on straight lines with slopes similar to that of the matrix material data. However,

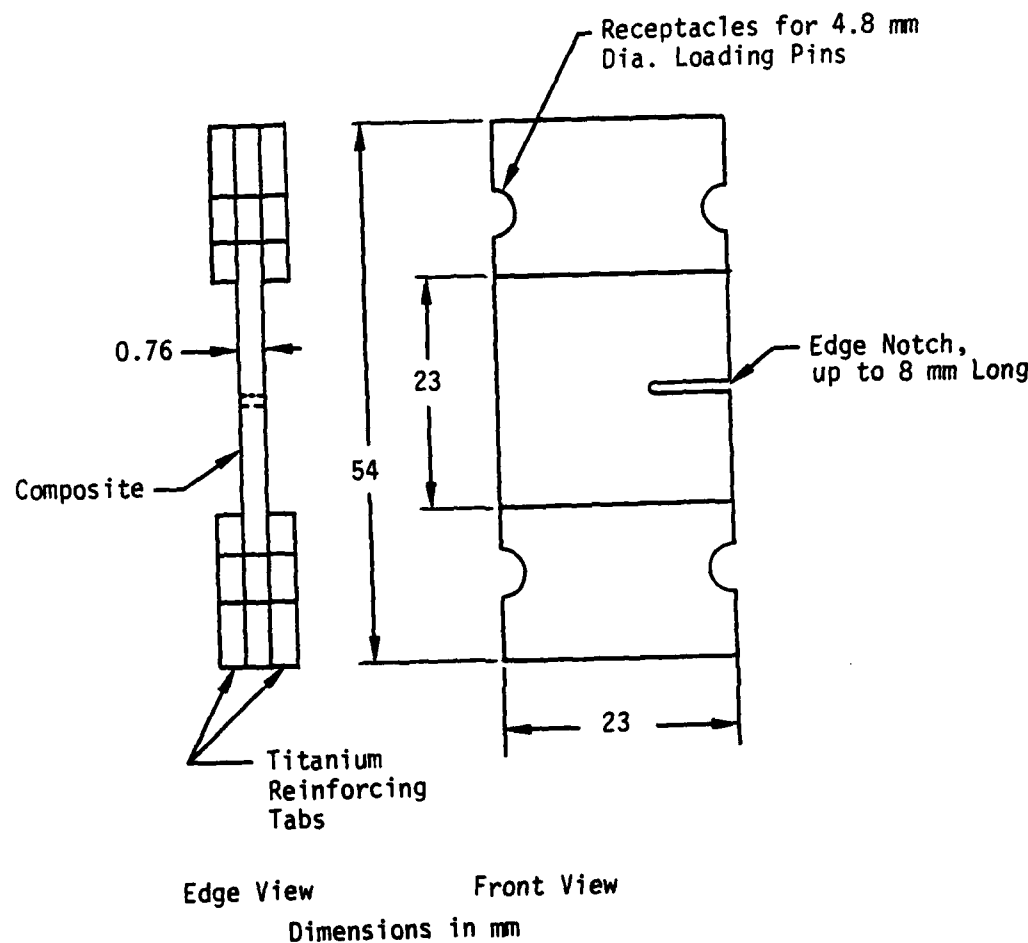
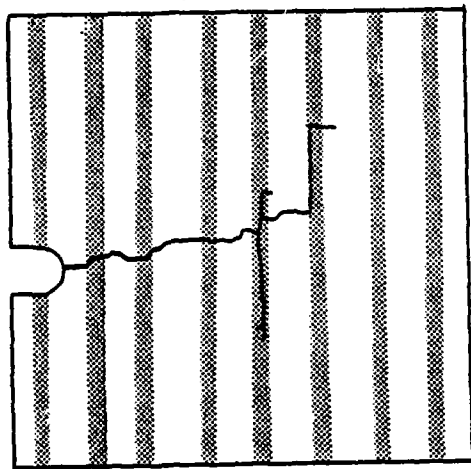


FIGURE 13. FATIGUE SPECIMEN.

As-Received
Room Temperature Test



Heat-Treated
(899°C 4.5 Hour Vac.)
Room Temperature Test

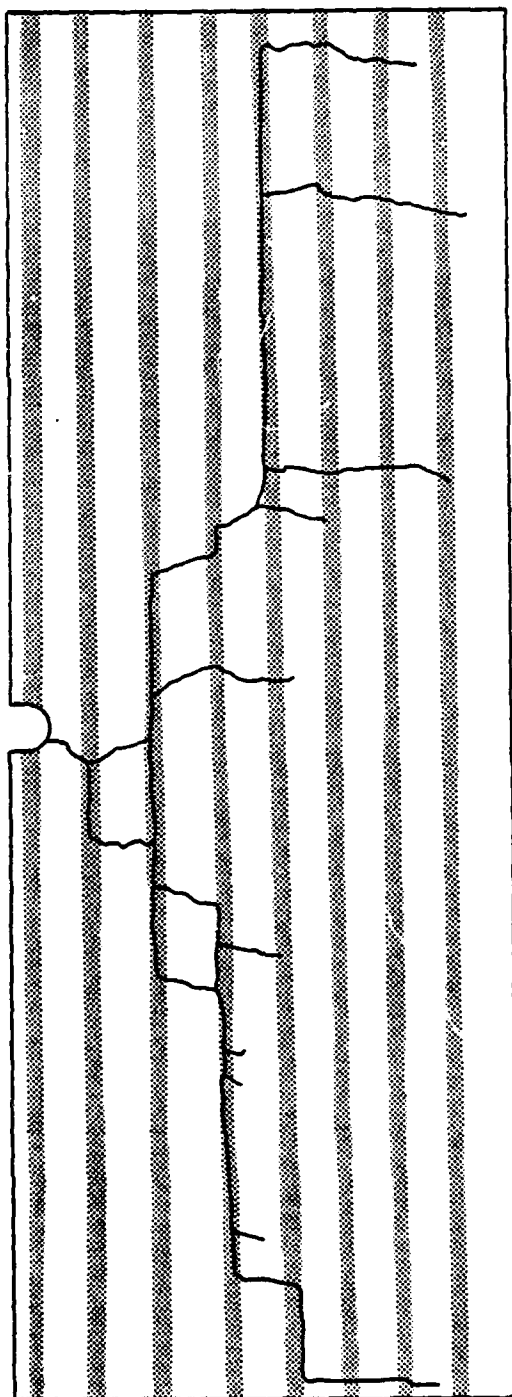


FIGURE 14. COMPARISON OF FATIGUE CRACK PATHS IN AS-RECEIVED AND HEAT-TREATED COMPOSITE SPECIMENS.

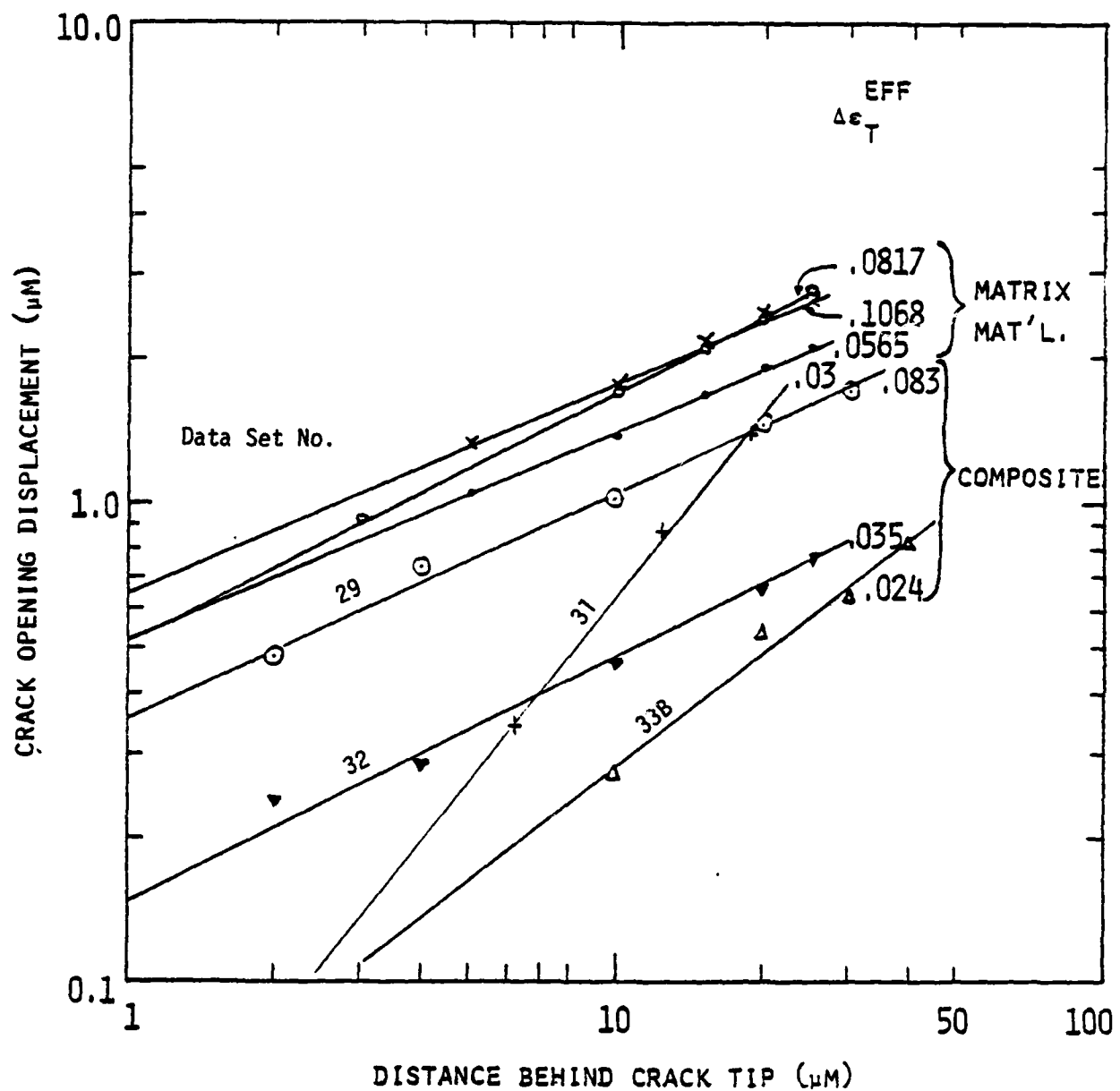


FIGURE 15. VARIATION OF CRACK OPENING DISPLACEMENT WITH DISTANCE BEHIND THE CRACK TIP. By comparing Data Set numbers with those in Table VIII and with Figure 16, position of the crack tip with respect to fibers may be determined.

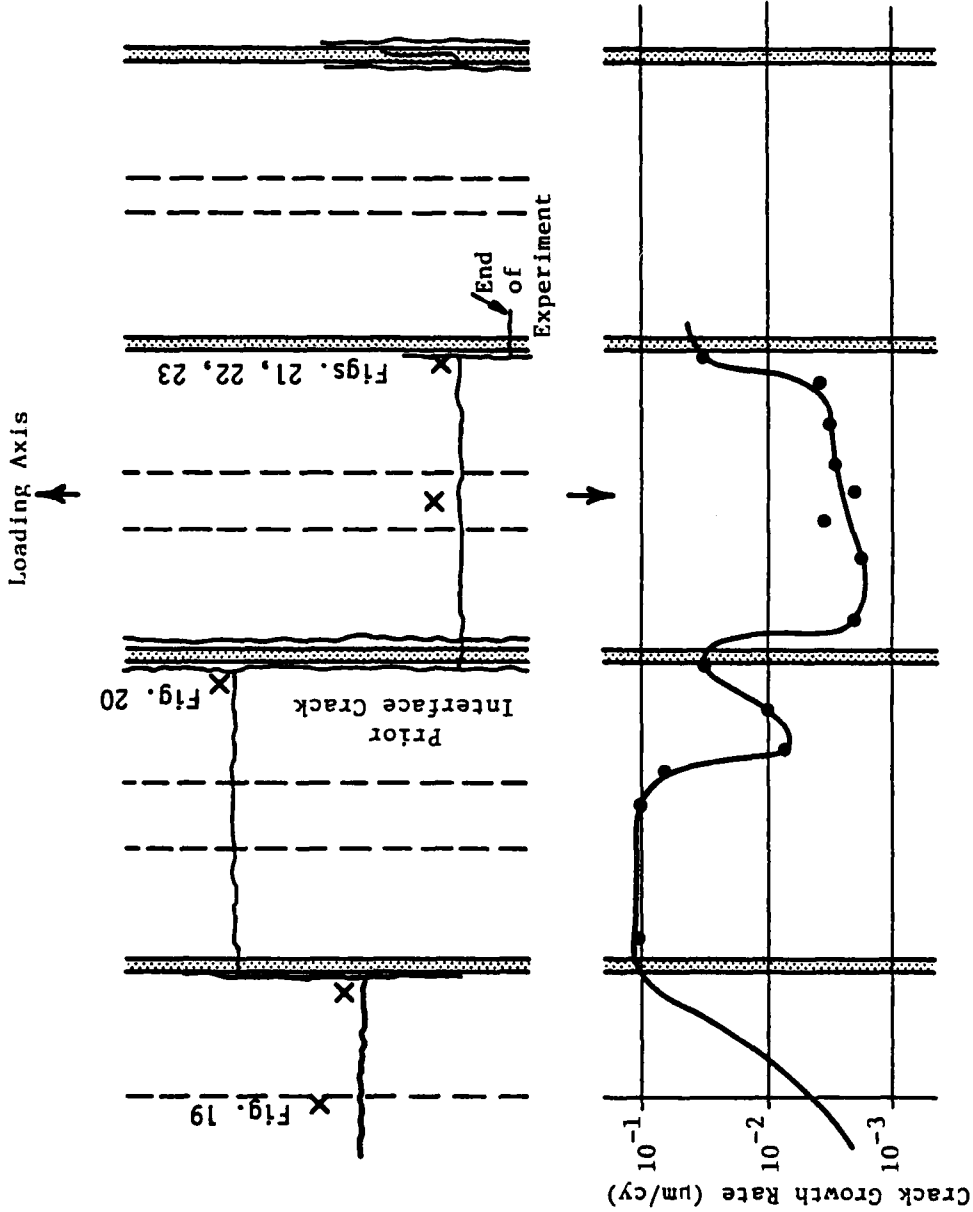


FIGURE 16. SCHEMATIC OF CRACK GROWTH THROUGH THE COMPOSITE, SHOWING MEASURED CRACK GROWTH RATES IN THE LOWER PORTION AND THE LOCATION OF SOME OF THE FOLLOWING FIGURES IN THE UPPER PORTION. Dotted lines indicate the position of the buried portion of the fiber, and the stippled region the visible part of the interface or fiber.

the displacements were reduced in the composite, so that these lines were below those of the matrix material. When the crack tip was near a fiber, the slope of the COD line was much steeper, reflecting the strong constraint imposed by the high-modulus fiber.

When the crack tip effective strain range data for the matrix material were plotted as a function of ΔK (Figure 17), they indicated a crack tip strain range proportional to $\Delta K^{2.8}$. By using this graph, the observed crack tip strain ranges of the composite were converted to effective ΔK levels experienced by the cracks in the composite when the applied ΔK was $22 \text{ MPa}\sqrt{\text{m}}$. Results of this procedure (Table VIII) show that the crack experiences only 5.8 to $9.4 \text{ MPa}\sqrt{\text{m}}$, considerably less than half the applied ΔK . Using the crack propagation data of Yuen et al., [10] these effective ΔK levels were used to predict crack propagation rates in the Ti-6Al-4V. As shown in Table VIII, the results are in excellent agreement with observed rates, except when the crack was near the debonded interface. This anomalous result is consistent with the modified crack opening result described above.

Figures 18-22 display the maximum shear strain ranges around crack tips, as determined by stereoimaging. The strains around a crack tip in unreinforced Ti-6Al-4V are shown in Figure 18. There is a strong concentration of strain at the crack tip, as expected. The strain range distribution around a crack in the composite, when the crack tip was remote from the fiber/matrix interface, was similar to the distribution in unreinforced material (Figure 19). Figure 20 shows the maximum shear strain ranges for a fatigue crack tip which was approaching a previously debonded interface. The cracked interface has clearly modified the strain distribution and reduced the degree of strain concentration (note the expanded vertical scale in this figure). Figure 21 reveals that the strain range distribution was also different when the crack was near an unbroken interface. Figure 22 relates to the same crack position as Figure 21. However, Figure 22 displays not the cyclic strain ranges, but the accumulated strains due to propagation of the crack into this area. The accumulated strains are comparable in magnitude to the cyclic strain ranges. Figure 23 shows the accumulated strains normal to the interface for the same analysis as shown in Figure 22. Along the interface the strains vary from tensile (positive) to compressive (negative). Debonding initiated in the central region of tensile strain, near a local maximum in the strain plot. The normal tensile strain at this point was about 0.2%; the maximum shear strain was about 2.5%.

It is clear from this year's results that the stereoimaging technique can measure critical strains to debonding. The SAM technique has proven capable of quantitative analysis of calcium segregation at the fiber/matrix interface, and has shown that heat treatment enhances this calcium segregation. What remains for the next year of the program is to apply the techniques to material given a heat treatment designed to produce a lesser degree of interface degradation. It will then be possible to quantitatively relate the critical strains to the interface chemistry.

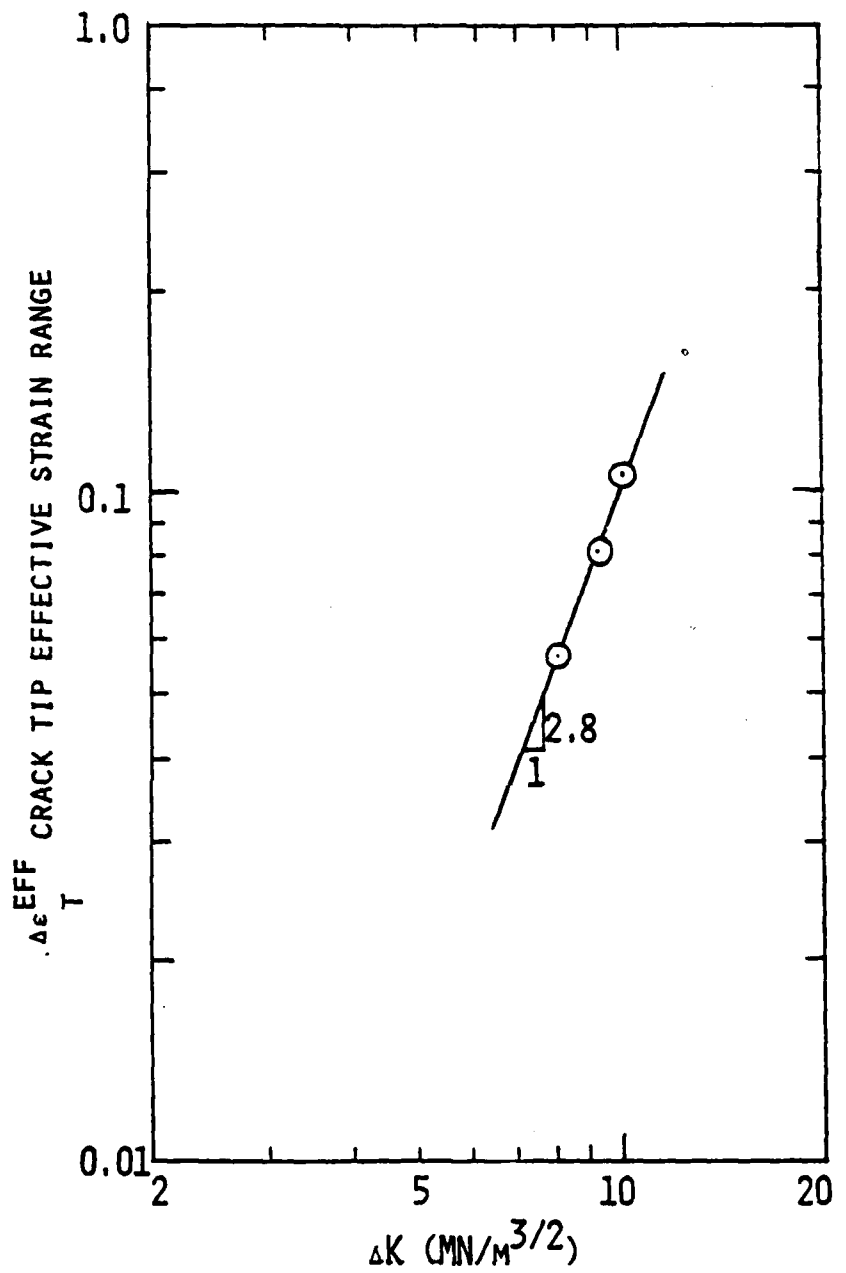


FIGURE 17. CYCLIC RANGE OF EFFECTIVE STRAIN AT THE TIP OF A FATIGUE CRACK IN UNREINFORCED Ti-6Al-4V, AS A FUNCTION OF THE APPLIED STRESS INTENSITY FACTOR RANGE.

TABLE VIII
EFFECTIVE ΔK EXPERIENCED BY CRACKS IN COMPOSITE AT
APPLIED ΔK OF 22 MPa \sqrt{m}

<u>Data Set</u>	<u>Location</u>	<u>$\Delta \epsilon_t^{eff}$</u>	<u>ΔK_{eff} (MPa\sqrt{m})</u>	<u>Predicted da/dN ($\mu m/cycle$)</u>	<u>Observed da/dN ($\mu m/cycle$)</u>
29	Remote from Fiber	.0832	9.4	2×10^{-2}	2×10^{-2}
32	Remote from Fiber	.0350	6.6	4.5×10^{-3}	4.5×10^{-3}
31	At Debonded Interface	.0299	6.4	4.5×10^{-3}	3.3×10^{-2}
33B	At Sound Interface	.0240	5.8	3×10^{-3}	3×10^{-3}

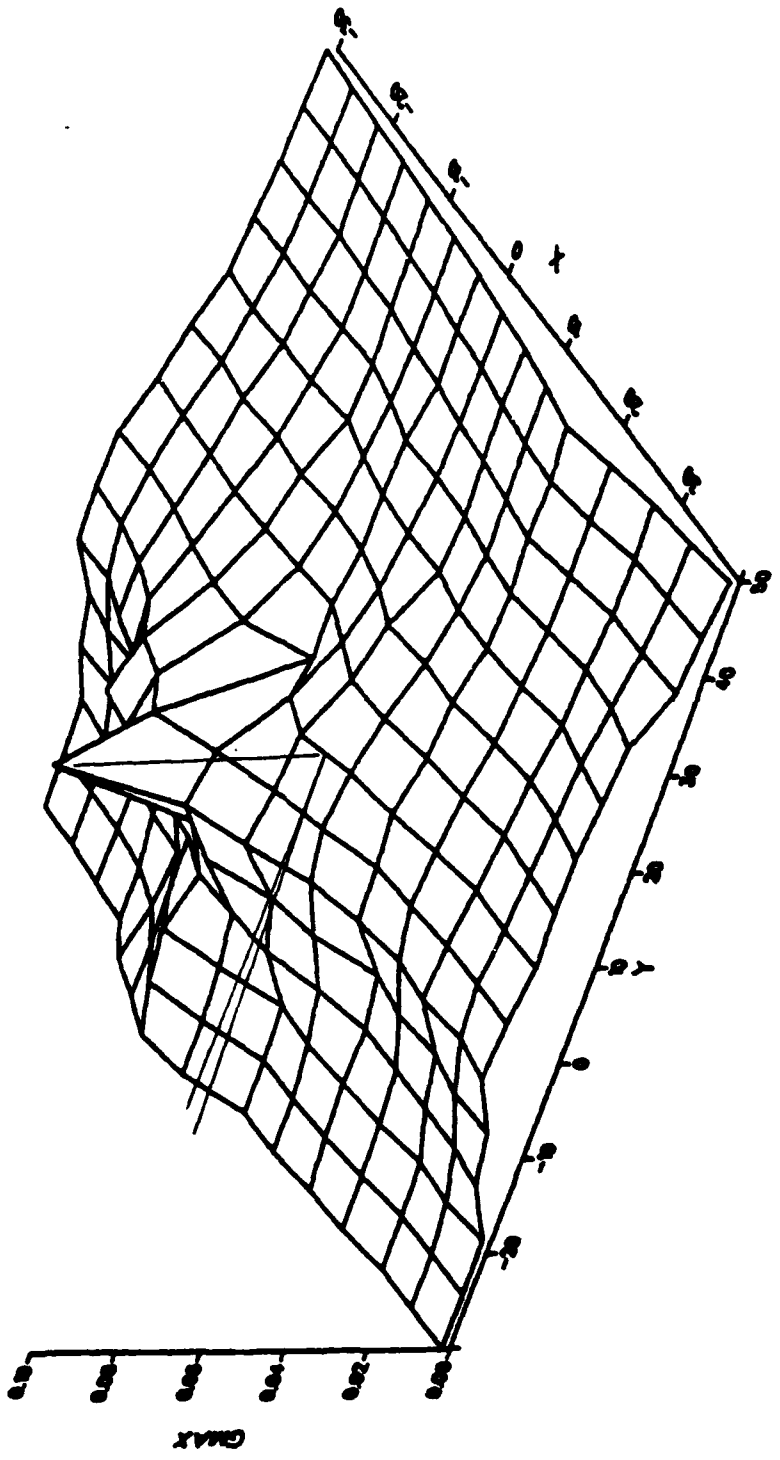


FIGURE 18. MAXIMUM SHEAR STRAIN RANGE DISTRIBUTION FOR A FATIGUE CRACK GROWN AT $\Delta K = 8 \text{ MN/m}^{3/2}$, DRY ENVIRONMENT, IN MATRIX MATERIAL; x AND y IN MICROMETERS. Crack is shown schematically on the zero strain surface.

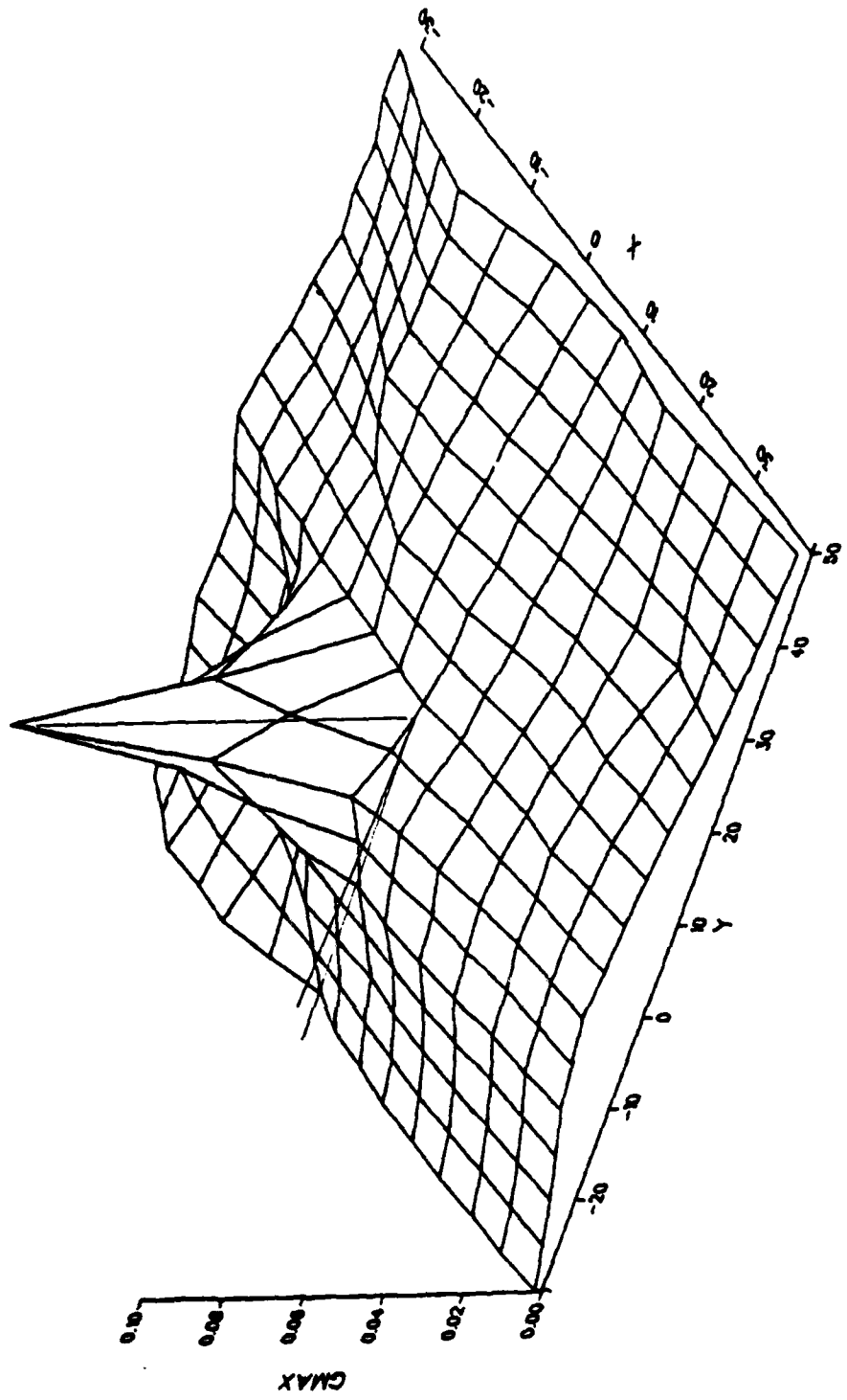


FIGURE 19. MAXIMUM SHEAR STRAIN RANGE DISTRIBUTION FOR A FATIGUE CRACK GROWN IN THE COMPOSITE; CRACK IS APPROXIMATELY 170 μm FROM FIBER. Note similarity of strain range distribution with matrix material; x and y in micrometers.

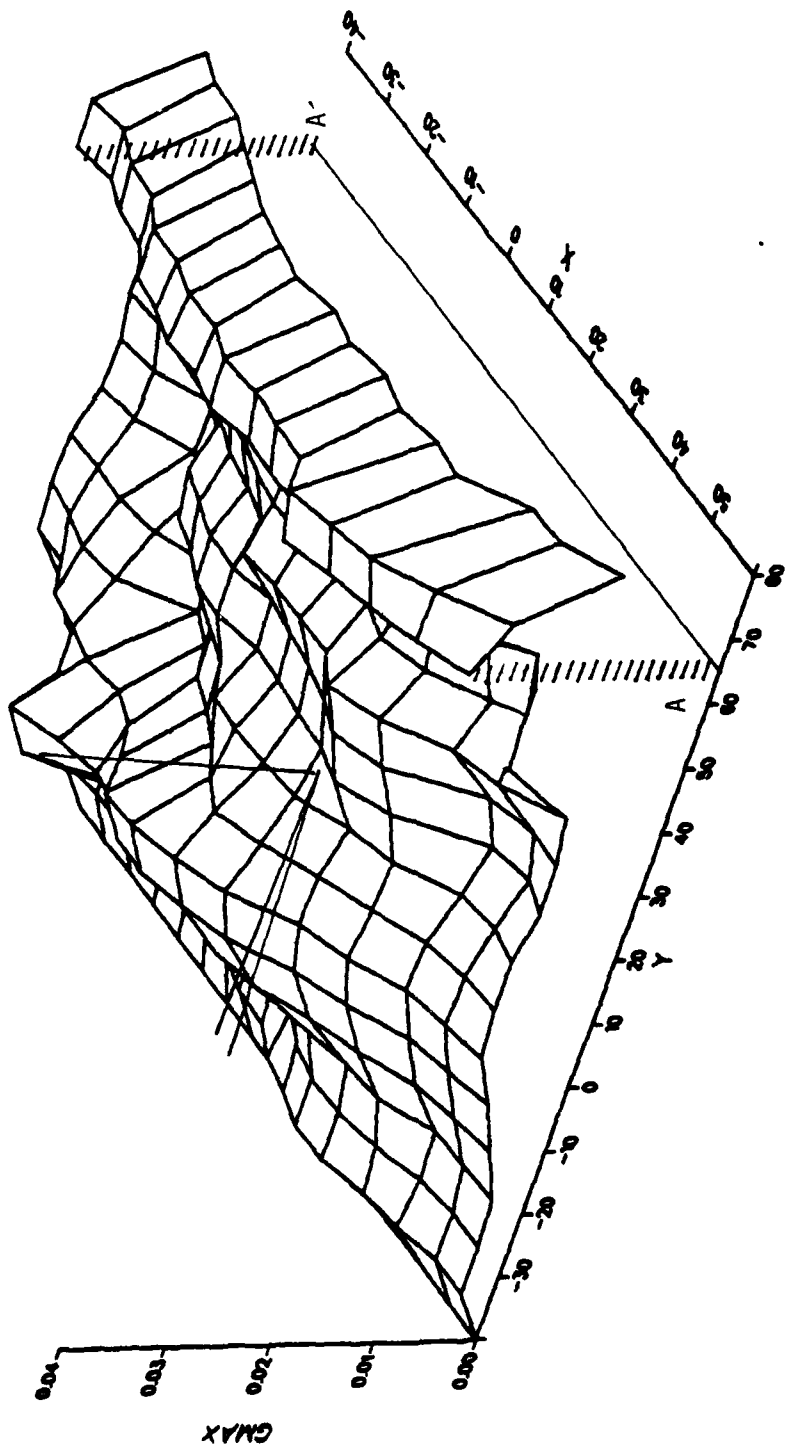


FIGURE 20. MAXIMUM SHEAR STRAIN RANGE DISTRIBUTION; FATIGUE CRACK APPROXIMATELY 60 μm FROM DEBONDED (CRACKED) INTERFACE, WHICH IS SHOWN BY THE LINES AT ABOUT $y = 60 \mu\text{m}$. Note that strain has been redistributed by the close proximity to the fiber interface. $A-A'$ is the surface trace of the interface.

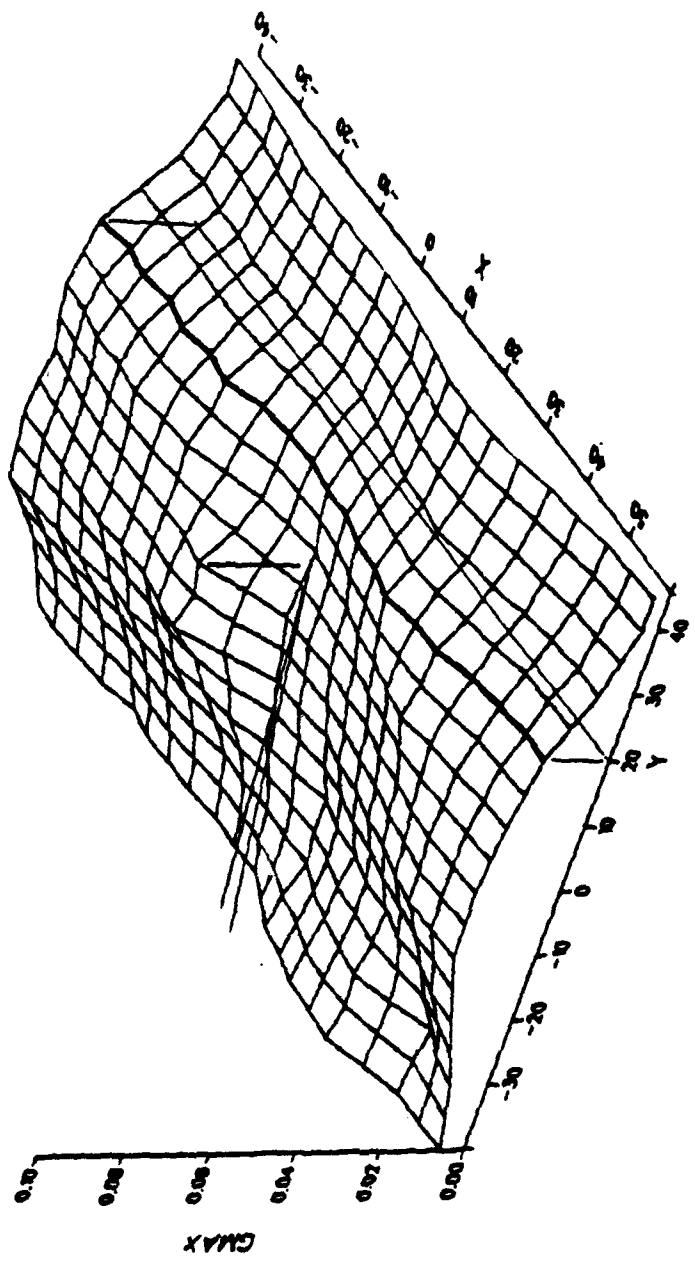


FIGURE 21. MAXIMUM SHEAR STRAIN RANGE DISTRIBUTION; CRACK TIP APPROXIMATELY 20 μm FROM AN UNCRACKED FIBER/MATRIX INTERFACE, SHOWN AS THE HEAVY LINE AT $y = 20 \mu\text{m}$. Note redistribution of strains in this figure, as compared to a crack well away from an interface.

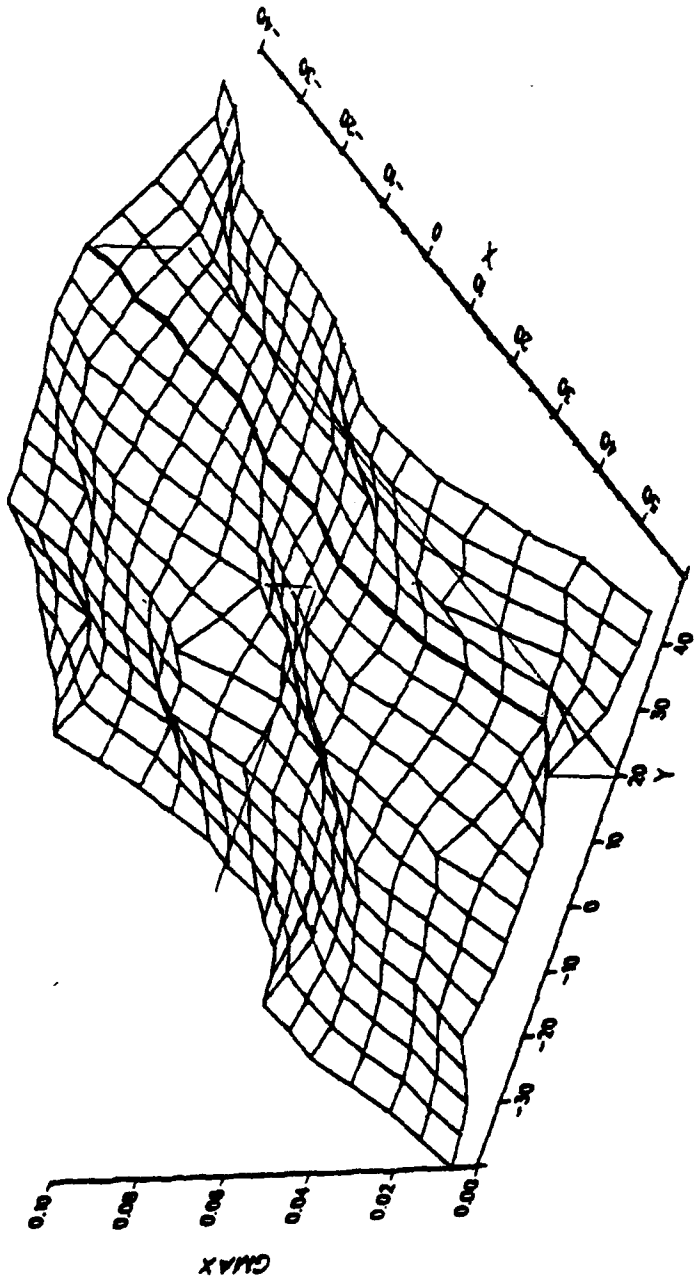


FIGURE 22. MAXIMUM SHEAR STRAIN WHICH HAS ACCUMULATED NEAR THE INTERFACE REGION, WHICH IS APPROXIMATELY 20 μm AHEAD OF THE CRACK TIP. The crack is depicted as closed because the strain distribution shown is for the unloaded crack as compared to uncracked material. This figure indicates the relatively large accumulation of strains which occur in the interfacial region just due to cyclic deformation; the magnitude of these cumulative strains is comparable to the cyclic strain range (Figure 21).

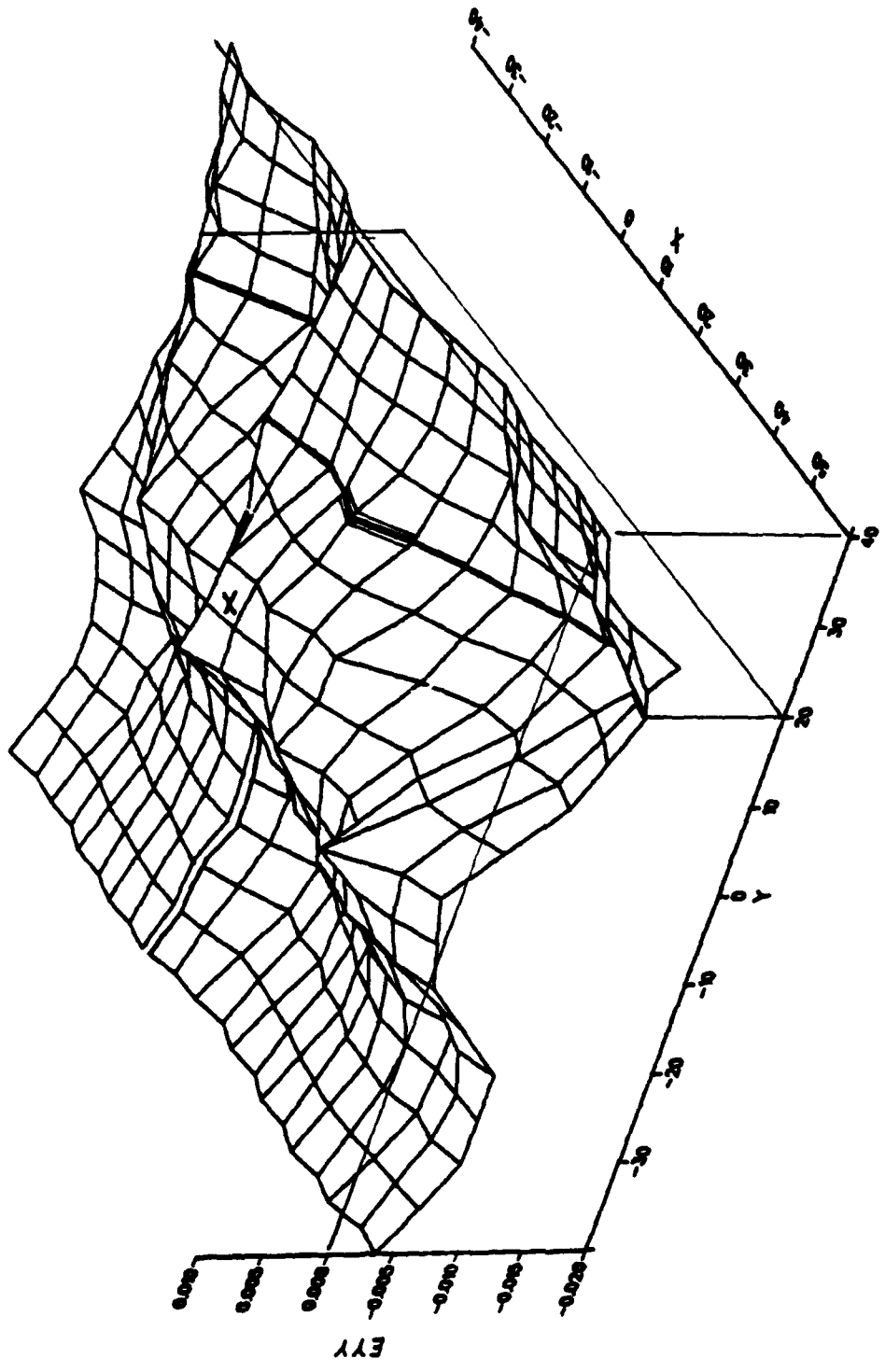


FIGURE 23. DISTRIBUTION OF CUMULATIVE y -AXIS STRAINS IN THE DIRECTION PERPENDICULAR TO THE INTERFACE (E_{YY}). The interface, approximately 20 μm ahead of the crack tip, is shown as a heavy black line. A small cross is shown on the E_{YY} = 0 plane at the crack tip ($x = 0, y = 0$). Note that these "debonding strains" are both negative (compressive) and positive (tensile) along the interface. Cracking along the interfacial boundary subsequently initiated along the region shown by the double lines in which the strains are slightly tensile.

5. References

- [1] Williams, D. R., Davidson, D. L., and Lankford, J., Experimental Mechanics, 20, 1980, p. 134.
- [2] Mahulikar, D. S., Air Force Office of Scientific Research Contract No. 80-0052, personal communication.
- [3] Rhodes, C. G., AFWAL Contract No. F33601-80-MN179, Final Report, March 1981.
- [4] Naslain, R., Thebault, J., and Pailler, R., in Proceedings of the 1975 International Conference on Composite Materials, E. Scala, E. Anderson, I. Toth and B. R. Noton, ed., AIME, 1976, p. 116.
- [5] Dolowy, J. F. Jr., Webb, B. A., and Harrigan, W. C., "Fiber Reinforced Titanium Composite Materials," 24th National SAMPE Meeting, San Francisco, May 1979.
- [6] Brewer, W. D., Unnam, J., and Tenney, D. R., "Mechanical Property Degradation and Chemical Interactions in a Borsic/Titanium Composite," 24th National SAMPE Meeting, San Francisco, May 1979.
- [7] Metcalfe, A. G., in Composite Materials, L. V. Broutman and R. H. Krock, eds., Academic Press, V. 1, 1974, p. 67.
- [8] Davis, L. E., MacDonald, N. C., Palmberg, P. W., Riach, G. E., and Weber, R. E., Handbook of Auger Electron Spectroscopy, Physical Electronics Division, Perkin-Elmer Corporation, Eden Prairie, MN, 1976, p. 13-15.
- [9] Burkstrand, J. M., Clough, S. P., Davidson, D. L., and Hack, J. E., in Scanning Electron Microscopy/1982, SEM, Inc. (in press).
- [10] Yuen, A., Hopkins, S. W., Leverant, G. R., and Rau, C. A., Metall. Trans., 5, 1974, p. 1833.

III. PUBLICATIONS (AFOSR SPONSORSHIP)

1. D. L. Davidson, "Electron Channeling: A New Metallurgical Tool," Research/Development, 25, 9, pp. 34-40, September 1974.
2. J. Lankford and J. G. Barbee, "SEM Characterization of Fatigue Crack Tip Deformation in Stainless Steel Using a Positive Replica Technique," Journal of Materials Science, 9, pp. 1906-1908, 1974.
3. D. L. Davidson, "Fatigue Crack Plastic Zone Size and Shape Through The Specimen Thickness," International Journal of Fracture, 11, pp. 1047-1048, 1975.
4. J. Lankford and D. L. Davidson, "Fatigue Crack Tip Plasticity Associated with Overloads and Subsequent Cycling," ASME Journal of Engineering Materials and Technology, 98(1), Series H, pp. 17-23, 1976.
5. D. L. Davidson and J. Lankford, "Plastic Strain Distribution at the Tips of Propagating Fatigue Cracks," ASME Journal of Engineering Materials and Technology, 98(1), Series H, pp. 24-29, 1976.
6. J. Lankford and D. L. Davidson, "Discussion of Plastic Zone Sizes in Fatigued Specimens of Inco 718," Metallurgical Transactions, A, 7A, p. 1044, 1976.
7. D. L. Davidson, "Applications of Electron Channeling to Materials Science," Proceedings, Electron Microscopy of America Annual Meeting, p. 402, 1976.
8. J. Lankford, D. L. Davidson, and T. S. Cook, "Fatigue Crack Tip Plasticity," Cyclic Stress-Strain and Plastic Deformation Aspects of Fatigue Crack Growth, ASTM STP 637, American Society for Testing and Materials, p. 36, 1977.
9. J. Lankford and D. L. Davidson, "Fatigue Crack Tip Plastic Zone Sizes in Aluminum Alloys," International Journal of Fracture, 14, p. R87, 1978.
10. D. L. Davidson, "The Study of Fatigue Mechanisms with Electron Channeling," Fatigue Mechanisms, ASTM STP 675, American Society for Testing and Materials, p. 254, 1979.
11. D. L. Davidson, "Fatigue Crack Tip Displacement Observations," Journal of Materials Science, 14, p. 231, 1979.

12. D. L. Davidson and J. Lankford, "Dynamic, Real-Time Fatigue Crack Propagation at High Resolution as Observed in the Scanning Electron Microscope," Fatigue Mechanisms, ASTM STP 675, American Society for Testing and Materials, p. 277, 1979.
13. D. L. Davidson, "The Observation and Measurement of Displacements and Strain by Stereoimaging," SEM/1979.
14. D. L. Davidson and J. Lankford, "Fatigue Crack Tip Plasticity Resulting From Load Interactions in an Aluminum Alloy," Fat. Eng. Mat. Struc., 1, p. 439, 1979.
15. D. L. Davidson and D. Eylon, "Titanium Alloy Fatigue Fracture Facet Investigation by Selected Area Electron Channeling," Met. Trans. A (in press).
16. J. Lankford and D. L. Davidson, "Effect of Aluminum Alloying on Fatigue Crack Tip Strain Fields," Met. Trans. A (in preparation).
17. D. R. Williams, D. L. Davidson, and J. Lankford, "Fatigue Crack Tip Plastic Strains by the Stereoimaging Technique," Experimental Mechanics, 20, p. 134, 1980.
18. D. L. Davidson and J. Lankford, "Fatigue Crack Propagation: New Tools for an Old Problem," Jour. Met., 31, p. 11, 1979.
19. J. Lankford and D. L. Davidson, "Effect of Overloads Upon Fatigue Crack Tip Opening Displacements and Strain Fields in Aluminum Alloys," Fracture 1981, p. 899, 1981.
20. J. E. Hack and G. R. Leverant, "A Model for Hydrogen-Assisted Crack Initiation on Planar Shear Bands in Near-Alpha Titanium Alloys," Scripta Met., 14, p. 437, 1980.
21. D. L. Davidson and J. Lankford, "Characterization of Crack Tip Plastic Zone Parameters and Their Interrelationship with NDE Techniques," Nondestructive Evaluation: Microstructural Characterization and Reliability Strategies, ed. O. Buck and S. M. Wolf, AIME, Warrendale, PA, p. 299, 1981.
22. D. L. Davidson and J. Lankford, "Fatigue Crack Tip Plastic Strain in High Strength Aluminum Alloys," Fatigue of Engineering Materials and Structures, 3, p. 289, 1980.
23. J. E. Hack and G. R. Leverant, "The Influence of Microstructure on the Susceptibility of Near-Alpha Titanium Alloys to Internal Hydrogen Embrittlement," (accepted for publication).
24. D. L. Davidson and J. Lankford, "Fatigue Crack Tip Strains in 7075-T6 by Stereoimaging and Their Use in Crack Growth Models," Quantitative Measurement of Fatigue Damage, ASTM STP (in press).

25. S. R. Bodner, D. L. Davidson and J. Lankford, "A Description of Fatigue Crack Growth in Terms of Plastic Work," Engineering Fracture Mechanics, 1982 (in press).
26. J. E. Hack, "Comments on 'An Electron Microscope Study of Hydrogen Embrittlement in Vanadium-II,'" Scripta Metallurgica, 15, p. 1057, 1981.
27. J. M. Burkstrand, S. P. Clough, D. L. Davidson, and J. E. Hack, "Effects of Thermal Exposure on Fiber-Matrix Interfacial Composition in a Titanium Matrix Composite," in Scanning Electron Microscopy/1982, SEM, Inc. (in press).
28. D. L. Davidson, R. Arrowood, J. E. Hack, and G. R. Leverant, "Micromechanisms of Crack Growth in a Fiber Reinforced Titanium Matrix Composite," to be published in the proceedings of "Failure Modes in Composites VI," held at the annual AIME Meeting, Dallas, TX, February 1982.

IV. PROGRAM PERSONNEL

Name	Title	
Dr. James Lankford	Staff Scientist	Co-principal Investigators
Dr. David L. Davidson	Staff Scientist	
Dr. Gerald R. Leverant	Assistant Director, Materials Sciences	
Mr. John Hack	Research Engineer	
Dr. Roy Arrowood	Senior Research Engineer	
Mr. Ronald McInnis	Senior Technician	
Mr. John Campbell	Technician	
Mr. Harold Saldana	Senior Technician	

V. INTERACTIONS (1981)

A. Aluminum Phase

1. Seminar - IBM, "Assessment of Defect Densities Using Selected Area Electron Channeling Patterns," San Jose, 9 Feb.
2. Lecture - Stanford Symposium (Northern California Soc. for Electron Microscopy), "The Assessment of Defect Density Magnitude by Changes in Selected Area Electron Channeling Patterns," Stanford, 12 Feb.
3. Seminar - Wright Patterson AFB, "Fatigue Crack Growth in Powder Metallurgy Materials," 1 June.
4. Paper - Soc. for Experimental Stress Analysis, "Fatigue Crack Tip Plasticity: Dynamic and Static Observations," Dearborn, 2 June.
5. Paper - Microbeam Analysis Society, "Crystallographic Contrast in the SEM," Vail, 13 July.
6. Lecture - ASM Meeting, Alamo Chapter, "Recent Studies in Crack Propagation," 15 Sept.
7. TMS-AIME - Louisville, Ky., "Fatigue Crack Response in 7075-T6 Due to a Single Overload: Dynamic and Static Analyses," 12 Oct.
8. Air Force Workshop on Powder Metallurgy Alloys, Louisville, Ky., "Crack Tip Plasticity in P/M Aluminum Alloys," 15 Oct.

B. Titanium Phase

1. We are currently in the process of correlating behavior of the Ti alloys with calculations of diffusion profiles of hydrogen in the stress gradient present at the tip of a stress concentration. These calculations are being performed on an internal research program at SwRI.
2. In-situ HVEM experiments at Oak Ridge National Laboratory are also being performed on an internal research program with the aim of defining the effects of hydrogen on the slip character and the effects of stress on the hydride solvus behavior in alpha-titanium.
3. Held discussions on the implications of the predictions of the embrittlement model for titanium alloys of interest to the Navy with personnel from NRC and NSRDC.

C. Titanium Matrix Composite Phase

1. J. E. Hack, D. L. Davidson, and G. R. Leverant, "Direct Observation of Fatigue Crack Tip Behavior in a B4C-Coated Boron Fiber Reinforced Titanium Composite," Fall Meeting, AIME, Louisville, 1981.
2. Meeting at Southwest Research Institute to discuss progress and exchange information on fatigue research on titanium matrix composites. Participants: D. L. Davidson, J. E. Hack, Roy Arrowood, and G. R. Leverant (SwRI); Harris Marcus, Deepak Mahulikar, and Young H. Park (University of Texas at Austin - AFOSR Contract No. 80-0052); and Alan Rosenstein (AFOSR).

END
DATE
FILMED

10.82

DTI